



**HAL**  
open science

# Molecular and Electronic Structure of Isolated Platinum Sites Enabled by the Expedient Measurement of $^{195}\text{Pt}$ Chemical Shift Anisotropy

Amrit Venkatesh, Domenico Giofrè, Benjamin A Atterberry, Lukas Rochlitz, Scott L Carnahan, Zhuoran Wang, Georges Menzildjian, Anne Lesage, Christophe Copéret, Aaron J Rossini

► **To cite this version:**

Amrit Venkatesh, Domenico Giofrè, Benjamin A Atterberry, Lukas Rochlitz, Scott L Carnahan, et al.. Molecular and Electronic Structure of Isolated Platinum Sites Enabled by the Expedient Measurement of  $^{195}\text{Pt}$  Chemical Shift Anisotropy. *Journal of the American Chemical Society*, 2022, 144 (30), pp.13511-13525. 10.1021/jacs.2c02300 . hal-04018980

**HAL Id: hal-04018980**

**<https://hal.science/hal-04018980v1>**

Submitted on 8 Mar 2023

**HAL** is a multi-disciplinary open access archive for the deposit and dissemination of scientific research documents, whether they are published or not. The documents may come from teaching and research institutions in France or abroad, or from public or private research centers.

L'archive ouverte pluridisciplinaire **HAL**, est destinée au dépôt et à la diffusion de documents scientifiques de niveau recherche, publiés ou non, émanant des établissements d'enseignement et de recherche français ou étrangers, des laboratoires publics ou privés.

This document is confidential and is proprietary to the American Chemical Society and its authors. Do not copy or disclose without written permission. If you have received this item in error, notify the sender and delete all copies.

**The Molecular and Electronic Structure of Isolated Platinum Sites Enabled by Expedient Measurement of  $^{195}\text{Pt}$  Chemical Shift Anisotropy**

Journal:	<i>Journal of the American Chemical Society</i>
Manuscript ID	ja-2022-02300g.R1
Manuscript Type:	Article
Date Submitted by the Author:	n/a
Complete List of Authors:	Venkatesh, Amrit; EPFL, Institute of Chemical Sciences and Engineering Gioffrè, Domenico; Eidgenössische Technische Hochschule Zurich, Department of Chemistry and Applied Biosciences Atterberry, Benjamin; Iowa State University, Department of Chemistry Rochlitz, Lukas; Eidgenössische Technische Hochschule Zurich, Department of Chemistry and Applied Biosciences Carnahan, Scott; Iowa State University, Chemistry Wang, Zhuoran; Very High Field NMR Center of Lyon, Menzildjian, Georges; EPFL, ISIC Lesage, Anne; Ecole normale supérieure de Lyon, High field NMR Center Copéret, Christophe; Eidgenössische Technische Hochschule Zurich, Department of Chemistry and Applied Biosciences; ETH Zurich, Rossini, Aaron; Iowa State University, Department of Chemistry

SCHOLARONE™  
Manuscripts

1  
2  
3  
4  
5  
6  
7  
8  
9  
10  
11  
12  
13  
14  
15  
16  
17  
18  
19  
20  
21  
22  
23  
24  
25  
26  
27  
28  
29  
30  
31  
32  
33  
34  
35  
36  
37  
38  
39  
40  
41  
42  
43  
44  
45  
46  
47  
48  
49  
50  
51  
52  
53  
54  
55  
56  
57  
58  
59  
60

# The Molecular and Electronic Structure of Isolated Platinum Sites Enabled by Expedient Measurement of $^{195}\text{Pt}$ Chemical Shift Anisotropy

*Amrit Venkatesh,<sup>1,2</sup> Domenico Gioffrè,<sup>3</sup> Benjamin A. Atterberry,<sup>1,2</sup> Lukas Rochlitz,<sup>3</sup> Scott L.  
Carnahan,<sup>1,2</sup> Zhuoran Wang,<sup>4</sup> Georges Menzildjian,<sup>4</sup> Anne Lesage,<sup>4\*</sup> Christophe Copéret,<sup>3\*</sup>  
Aaron J. Rossini<sup>1,2\*</sup>*

<sup>1</sup>*Iowa State University, Department of Chemistry, Ames, IA, USA, 50011*

<sup>2</sup>*US DOE Ames Laboratory, Ames, Iowa, USA, 50011*

<sup>3</sup>*Department of Chemistry and Applied Biosciences, ETH Zürich, CH-8093 Zürich, Switzerland.*

<sup>4</sup>*Univ Lyon, ENS Lyon, Université Lyon 1, CNRS, High-Field NMR Center of Lyon, UMR 5082, F-69100 VILLEURBANNE, France.*

## **Corresponding Authors**

\*e-mail: [anne.lesage@ens-lyon.fr](mailto:anne.lesage@ens-lyon.fr)

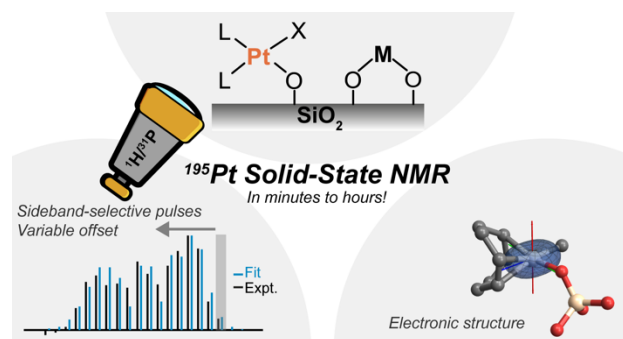
\*e-mail: [ccoperet@ethz.ch](mailto:ccoperet@ethz.ch)

\*e-mail: [arossini@iastate.edu](mailto:arossini@iastate.edu)

## Abstract

Techniques that can characterize the molecular structures of dilute surface species are required to facilitate the rational synthesis and improvement of Pt-based heterogeneous catalysts.  $^{195}\text{Pt}$  solid-state NMR spectroscopy could be an ideal tool for this task because  $^{195}\text{Pt}$  isotropic chemical shifts and chemical shift anisotropy (CSA) are highly sensitive probes of the local chemical environment and electronic structure. However, characterization of Pt surface-sites is complicated by the typical low Pt loadings that are between 0.2 to 5 wt.% and broadening of  $^{195}\text{Pt}$  solid-state NMR spectra by CSA. Here, we introduce a set of solid-state NMR methods that exploit fast MAS and indirect detection using a sensitive spy nucleus ( $^1\text{H}$  or  $^{31}\text{P}$ ) to enable rapid acquisition of  $^{195}\text{Pt}$  MAS NMR spectra. We demonstrate that high-resolution wide-line  $^{195}\text{Pt}$  MAS NMR spectra can be acquired in minutes to a few hours for a series of molecular and single-site Pt species grafted on silica with Pt loading of only 3-5 wt.%. Low-power, long-duration, sideband-selective excitation and saturation pulses are incorporated into  $t_1$ -noise eliminated (TONE) dipolar heteronuclear multiple quantum coherence (D-HMQC), perfect echo resonance echo saturation pulse double resonance (PE RESPDOR) or  $J$ -resolved pulse sequences. The complete  $^{195}\text{Pt}$  MAS NMR spectrum is then reconstructed by recording a series of 1D NMR spectra where the offset of the  $^{195}\text{Pt}$  pulses is varied. Analysis of the  $^{195}\text{Pt}$  MAS NMR spectra yields the  $^{195}\text{Pt}$  chemical shift tensor parameters. Zeroth order approximation (ZORA) DFT calculations accurately predict  $^{195}\text{Pt}$  CS tensor parameters. Simple and predictive orbital models relate the CS tensor parameters to the Pt electronic structure and coordination environment. The methodology developed here paves the way for the detailed structural and electronic analysis of dilute platinum surface-sites.

## TOC Graphic



## Introduction

Heterogeneous catalysis is widely used in industrial chemistry and is vital to sustainable chemical processes.<sup>1-5</sup> Recently, single-site<sup>6-7</sup> and single-atom<sup>8</sup> catalysts have emerged as a distinct class of highly efficient heterogeneous catalysts that display unique reactivity, increased catalytic efficiency and improved precious metal utilization. The ultimate goal in catalysis science is to derive detailed structure-activity relationship for rational development. The search for single-site catalysts that comprise of a well-defined coordination environment has thus been an active field of research. In this context, Surface Organometallic Chemistry (SOMC) has emerged as a powerful approach that relies on the controlled reaction of tailored molecular precursors with the functionality of supports, such as the isolated OH groups of oxide materials.<sup>9-11</sup> These well-defined surface species can be used directly as single-site catalysts or as precursors to i) generate isolated metal sites with defined oxidation state and nuclearity, or ii) control the interface, growth and composition of supported nanoparticles.<sup>12-16</sup> A key aspect of SOMC is the need to obtain an atomic-level characterization of surface species, using in particular solid-state nuclear magnetic resonance (NMR) spectroscopy.<sup>5, 17-23</sup>

Solid-state NMR spectroscopy has been used to determine the three-dimensional structure of surface single-sites with a sub-angstrom precision.<sup>24-25</sup> The complete measurement of the NMR chemical shift tensor via determination of the isotropic chemical shift and the chemical shift anisotropy (CSA) provides a fingerprint of the electronic structure and symmetry of an atomic environment.<sup>26-29</sup> For example, differences in magnitude of the CSA (the span), determined experimentally, and the computed orientation of the chemical shift tensors can be traced back to specific molecular frontier orbitals and their relative energies in organometallic complexes; this has been used for instance to predict the reactivity of alkene and alkyne metathesis catalysts,<sup>30-34</sup>

1  
2  
3 unravel the electronic structure of organo-tellurides<sup>35</sup> and understand the  $\pi$ -accepting abilities of  
4  
5 carbenes.<sup>36-38</sup> Many metal-based catalysts have spin-1/2 isotopes which can be directly probed by  
6  
7 solid-state NMR spectroscopy (<sup>89</sup>Y, <sup>103</sup>Rh, <sup>109</sup>Ag, <sup>113</sup>Cd, <sup>119</sup>Sn, <sup>183</sup>W, <sup>199</sup>Hg, <sup>195</sup>Pt, <sup>207</sup>Pb, etc.).  
8  
9  
10 However, direct NMR experiments on the metal nucleus of supported catalysts are challenging  
11  
12 because of the typically low metal loadings. Consequently, NMR experiments have traditionally  
13  
14 been limited to highly receptive isotopes of metals such as aluminum,<sup>39</sup> scandium,<sup>21</sup> vanadium,<sup>40-</sup>  
15  
16 <sup>41</sup> niobium<sup>18</sup> and/or isotopically enriched materials.<sup>22, 42-43</sup> Recently, sensitivity-enhancement by  
17  
18 dynamic nuclear polarization (DNP) or proton detection has enabled NMR experiments on  
19  
20 catalysts featuring unreceptive nuclei.<sup>44-49</sup>  
21  
22  
23

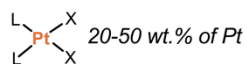
24 The noble metal platinum is utilized in numerous catalytic processes.<sup>8, 50-52</sup> However, Pt(II)  
25  
26 sites typically adopt a square-planar geometry, giving rise to very large <sup>195</sup>Pt CSA, reaching several  
27  
28 thousand ppm and making acquisition of <sup>195</sup>Pt solid-state NMR spectra challenging.<sup>53-55</sup> Yet,  
29  
30 measurement of <sup>195</sup>Pt isotropic chemical shifts and CSA provides invaluable information by  
31  
32 providing direct insight into the identity and symmetry of atoms within the Pt coordination sphere  
33  
34 as well as a full understanding of its electronic structure.<sup>55-60</sup> Towards this goal, various schemes  
35  
36 have been proposed for the acquisition of wideline solid-state NMR spectra.<sup>53, 61-63</sup> DNP has been  
37  
38 used to enhance further the sensitivity of wideline solid-state NMR experiments under static<sup>46, 64-</sup>  
39  
40 <sup>65</sup> and moderate magic angle spinning (MAS) conditions.<sup>49</sup> However, these methods offer poor  
41  
42 <sup>195</sup>Pt NMR resolution. Recently, we used static DNP experiments to characterize a model Pt single-  
43  
44 site catalyst at 3.7 wt.% Pt loading, however even with DNP, six days of acquisition time was  
45  
46 required to measure the <sup>195</sup>Pt CSA.<sup>66</sup> A rapidly developing approach to improve the sensitivity and  
47  
48 resolution of solid-state NMR experiments, which can be readily applied with standard solid-state  
49  
50 NMR spectrometers, is indirect detection of insensitive nuclei under fast MAS.<sup>67-70</sup>  
51  
52  
53  
54  
55  
56  
57  
58  
59  
60

1  
2  
3 In this work, we demonstrate that  $^{195}\text{Pt}$  chemical shift tensors can be measured with high  
4 resolution in only minutes to hours for a series of molecular and single-site Pt species grafted on  
5 silica with Pt loading of only 3-5 wt.% (Figure 1). Our approach consists in the incorporation of  
6 long duration, low-power, sideband-selective pulses into indirect detection  $^1\text{H}\{^{195}\text{Pt}\}$   $t_1$ -noise  
7 eliminated heteronuclear multiple quantum coherence (TONE D-HMQC), perfect echo resonance  
8 echo saturation pulse double resonance (PE RESPDOR) and  $^{31}\text{P}\{^{195}\text{Pt}\}$   $J$ -resolved or  $J$ -HMQC  
9 pulse sequences all of which are performed with fast MAS ( $\nu_{\text{rot}} \geq 25$  kHz). By varying the offset  
10 of the sideband-selective pulses across the  $^{195}\text{Pt}$  spectrum and monitoring the 1D NMR signal  
11 intensity, complete  $^{195}\text{Pt}$  NMR spectra can be obtained with sensitivity far exceeding that offered  
12 by traditional methods. These schemes, together with DFT computations, were applied to unravel  
13 the molecular and electronic signatures of surface Pt species. The large variations in experimental  
14  $^{195}\text{Pt}$  CSA can be related to simple orbital models, rationalizing the effect of different coordination  
15 environments on  $^{195}\text{Pt}$  CSA patterns.  
16  
17  
18  
19  
20  
21  
22  
23  
24  
25  
26  
27  
28  
29  
30  
31  
32  
33  
34  
35  
36  
37  
38  
39  
40  
41  
42  
43  
44  
45  
46  
47  
48  
49  
50  
51  
52  
53  
54  
55  
56  
57  
58  
59  
60



## A) Characterization of Pt metal sites

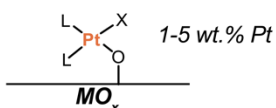
### Molecular System



### Characterization

- $^{195}\text{Pt}$  NMR ✓
- Single Crystal XRD ✓

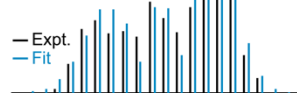
### Supported Pt Metal Sites



- Low Metal Content,
- Disorder & Large
- Chemical Shift Anisotropy

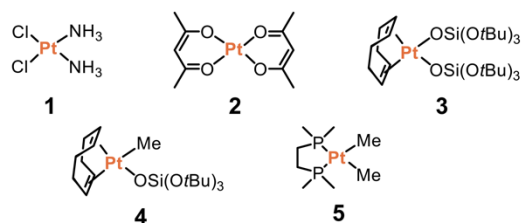
### This Work:

Few hours



- Rapid Structure
- Determination by  $^{195}\text{Pt}$
- Solid-State NMR

## B) Benchmark and Molecular Precursors



## C) Supported Single-Site Materials

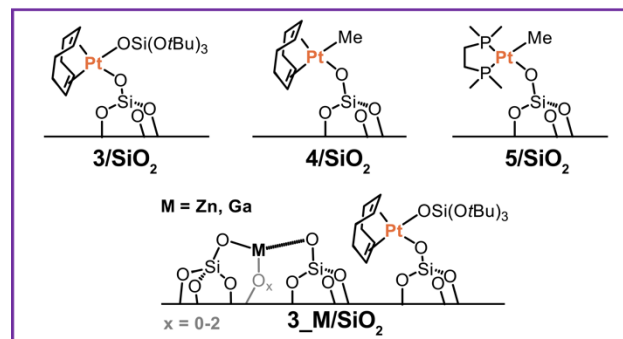


**Figure 1.** (A) Graphical summary of the characterization of molecular and supported Pt metal sites and the development of methodology for fast structure determination using  $^{195}\text{Pt}$  solid-state NMR. Scheme showing the structures of the (B) molecular and (C) supported single-site Pt compound studied in this work. The Pt loadings of the supported compounds were 3.73 wt.% (**3/SiO<sub>2</sub>**), 2.77 wt.% (**3\_Zn/SiO<sub>2</sub>**), 4.37 wt.% (**3\_Ga/SiO<sub>2</sub>**), 4.96 wt.% (**4/SiO<sub>2</sub>**) and 4.39 wt.% (**5/SiO<sub>2</sub>**).

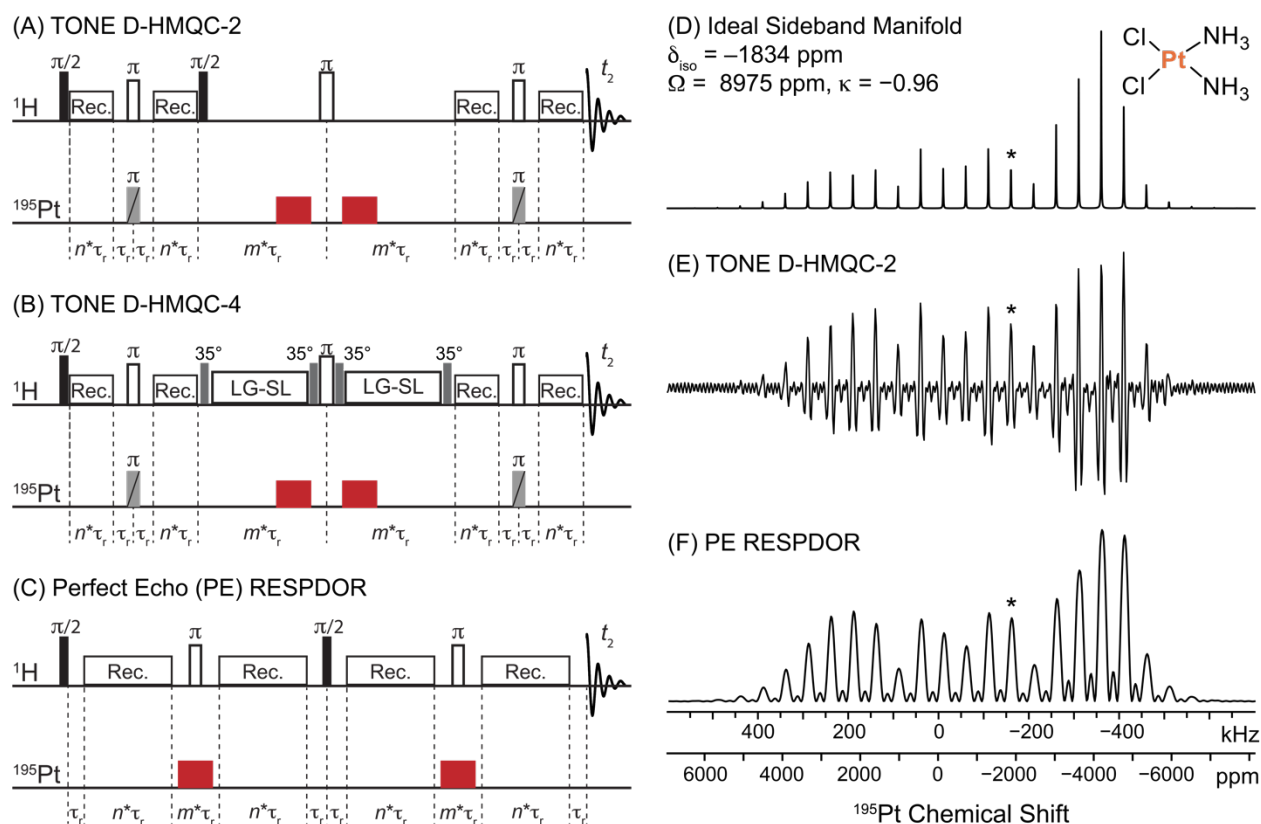


**Figure 2.**  $^1\text{H}\{^{195}\text{Pt}\}$  (A) TONE D-HMQC-2, (B) TONE D-HMQC-4 and (C) Perfect echo (PE) RESPDOR pulse sequences with low-rf field, sideband-selective excitation/saturation pulses with durations of one or more rotor cycles on the  $^{195}\text{Pt}$  channel denoted as red rectangles.  $m$  and  $n$  are positive integers and  $\tau_r$  denotes a rotor period. (D-F) Simulations of MAS  $^{195}\text{Pt}$  NMR spectra of cisplatin at 50 kHz MAS and  $B_0 = 9.4$  T using the previously reported  $^{195}\text{Pt}$  isotropic shift and CSA parameters (span ( $\Omega$ ) and skew ( $\kappa$ )). (D) Ideal simulation. Numerical SIMPSON simulations of sideband intensities obtained by varying the offset in steps of 1 kHz of 60  $\mu\text{s}$   $^{195}\text{Pt}$  sideband-selective (9 kHz rf field) excitation or saturation pulses within (E) TONE D-HMQC or (F) PE RESPDOR pulse sequences, respectively. The isotropic shift is indicated by an asterisk.

## Results and Discussion

*Sideband-Selective  $^{195}\text{Pt}$  NMR methods.* Wideline  $^1\text{H}\{^{195}\text{Pt}\}$  D-HMQC experiments<sup>71-74</sup> use microsecond duration, high-rf field ( $\nu_1 > 150$  kHz) excitation pulses to excite the broad  $^{195}\text{Pt}$  NMR spectra. Small rotor-asynchronous  $t_1$ -increments ( $\Delta t_1 < 4$   $\mu\text{s}$ ) are used to finely sample the indirect dimension time domain signal, allowing observation of the entire wideline  $^{195}\text{Pt}$  MAS spectrum in the frequency domain after 2D Fourier transformation.<sup>71-74</sup> However, when the indirect dimension spectrum consists of a series of sidebands due to a significant CSA, the sensitivity of the wideline NMR experiment is significantly reduced (Figure S1), and further

1  
2  
3 attenuated by  $t_1$ -noise. Recently Paluch *et al.* showed that the traditional microsecond duration,  
4 high-rf field excitation pulses used in  $^1\text{H}\{^{195}\text{Pt}\}$  D-HMQC experiments on samples with large CSA  
5 can be replaced with low-rf field pulses (5-50 kHz) with durations of one rotor cycle or longer.<sup>75</sup>  
6  
7 These multiple rotor cycle duration pulses have a narrow excitation bandwidth and must be applied  
8 on resonance with an isotropic peak or sideband; hence, we denote these pulses as being sideband-  
9 selective. Here, sideband-selective excitation or saturation  $^{195}\text{Pt}$  pulses are incorporated into D-  
10 HMQC and RESPDOR pulse sequences. To obtain the MAS  $^{195}\text{Pt}$  solid-state NMR spectra, a  
11 series of 1D sideband-selective D-HMQC or RESPDOR experiments are performed where the  
12  $^{195}\text{Pt}$  pulse offset frequency is stepped in increments equal to the MAS frequency. By plotting the  
13 1D NMR signal intensities as a function of the  $^{195}\text{Pt}$  pulse offset the MAS  $^{195}\text{Pt}$  NMR spectrum  
14 can be reconstructed (Figure 2 and Figure S2-S4). This method is analogous to previous work that  
15 utilized indirect detection schemes such as TRAPDOR,<sup>76-77</sup> REAPDOR,<sup>78</sup> RESPDOR<sup>79-80</sup> or  
16 PROSPR<sup>81</sup> where the signal dephasing of the detected nucleus at different transmitter offsets was  
17 used to reconstruct the NMR spectrum of the indirectly detected spin.  
18  
19  
20  
21  
22  
23  
24  
25  
26  
27  
28  
29  
30  
31  
32  
33  
34

35 Figure 2D shows the simulated ideal MAS  $^{195}\text{Pt}$  NMR spectrum of cisplatin, based on the  
36 previously reported CSA parameters  $\delta_{\text{iso}} = -1834$  ppm,  $\Omega = 8975$  ppm and  $\kappa = -0.96$ ,<sup>60, 71</sup> where  
37  $\delta_{\text{iso}}$ ,  $\Omega$  and  $\kappa$  denote the isotropic chemical shift, span and skew of the chemical shift tensor,  
38 respectively. Numerical SIMPSON<sup>82-84</sup> simulations show the effects of varying the offset of 60  $\mu\text{s}$ ,  
39 9 kHz rf field  $^{195}\text{Pt}$  pulses in 2 kHz steps for the TONE D-HMQC-2 and PE RESPDOR pulse  
40 sequences with  $SR4_1^2$  recoupling<sup>85</sup> (Figure 2E and 2F). Most importantly, a comparison of Figure  
41 2E and 2F with Figure 2D shows that the MAS  $^{195}\text{Pt}$  NMR spectrum is essentially reproduced in  
42 both cases, with peak intensities obtained with the PE RESPDOR sequence being very similar to  
43 the ideal spectrum (Figure 2D). Further details on sideband-selective NMR experiments and  
44  
45  
46  
47  
48  
49  
50  
51  
52  
53  
54  
55  
56  
57  
58  
59  
60

1  
2  
3 simulations are found in the SI for the interested reader (Figure S5-S11, Note S1), and will be  
4 elaborated on in a forthcoming publication. Note that the simulations and experiments shown in  
5 Figure 2 and 3 used  $t_1$ -noise eliminated (TONE) D-HMQC<sup>86</sup> and the closely related perfect echo<sup>87</sup>  
6 (PE) RESPDOR pulse sequences (Figure 2). Both of these sequences give more reliable <sup>1</sup>H NMR  
7 signal intensities because they are designed to tolerate experimental MAS frequency  
8 fluctuations.<sup>86, 88-89</sup> The use of PE RESPDOR to accurately measure heteronuclear distances is  
9 discussed elsewhere.<sup>90</sup>  
10  
11  
12  
13  
14  
15  
16  
17  
18  
19  
20  
21  
22  
23  
24  
25  
26  
27  
28  
29  
30  
31  
32  
33  
34  
35  
36  
37  
38  
39  
40  
41  
42  
43  
44  
45  
46  
47  
48  
49  
50  
51  
52  
53  
54  
55  
56  
57  
58  
59  
60

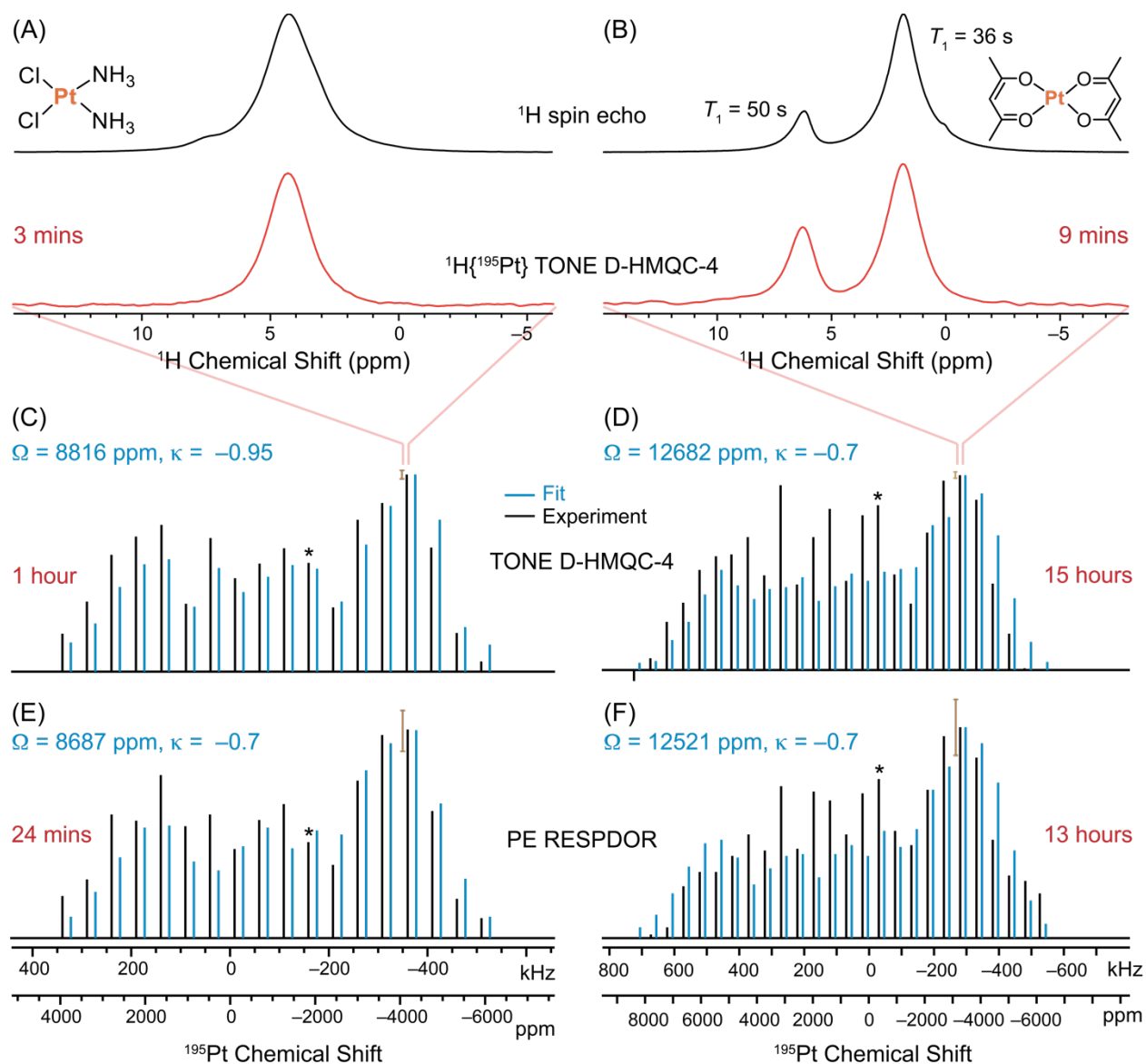


**Figure 3.** (A-B, upper traces) 1D  $^1\text{H}$  spin echo spectra. (A-F)  $^1\text{H}\{^{195}\text{Pt}\}$  sideband-selective solid-state NMR experiments on (A, C, E) cisplatin (**1**) and (B, D, F)  $\text{Pt}(\text{acac})_2$  (**2**) performed with a 50 kHz MAS frequency. (A-B, lower traces) 1D  $^1\text{H}\{^{195}\text{Pt}\}$  sideband-selective TONE D-HMQC-4 with the  $^{195}\text{Pt}$  transmitter applied at the most-intense sideband. (black traces) Sideband intensities from  $^1\text{H}\{^{195}\text{Pt}\}$  (C-D) TONE D-HMQC-4 and (E-F) PE RESPDOR experiments using  $60\ \mu\text{s}$ , 9 kHz rf field sideband-selective  $^{195}\text{Pt}$  pulses. For **2**, the signal intensities of the CH proton at 6.3 ppm are shown. (blue traces) SIMPSON simulated peak intensities corresponding to the indicated CS tensor parameters which gave the lowest RMSD. Error bars are provided only for the most intense sideband as the same magnitude of error applies to all sidebands (see SI for details on error bars). Total experiment times are indicated in red.

*Experimental Demonstration of  $^{195}\text{Pt}$  Sideband-Selective NMR Experiments on Molecular Precursors.* We tested sideband-selective  $^1\text{H}\{^{195}\text{Pt}\}$  TONE D-HMQC-4 and PE RESPDOR experiments with the two prototypical molecular compounds cisplatin (**1**) and  $\text{Pt}(\text{acac})_2$  (**2**) (Figure

1  
2  
3 3). The sideband-selective pulses must be applied precisely on-resonance with a  $^{195}\text{Pt}$  NMR signal.  
4  
5 The position of a sideband can be located using a high sensitivity rotor-synchronized D-HMQC  
6 experiment<sup>66, 73, 75</sup> or by varying the offset of the sideband-selective pulses in steps of 1-2 kHz,  
7  
8 until the signal (or dephasing) is observed; the former approach was employed throughout this  
9  
10 work. For both **1** and **2**, plots of the  $^1\text{H}\{^{195}\text{Pt}\}$  TONE D-HMQC-4 signal or the PE RESPDOR  
11  
12 dephasing as a function of the sideband-selective pulse offset yields the intensity of each sideband  
13  
14 in the MAS  $^{195}\text{Pt}$  NMR spectrum.  
15  
16  
17  
18

19 For both types of NMR experiments CSA parameters were determined by least-squares  
20 fitting of the sideband intensities using SIMPSON simulations (Figure S12). The resulting CSA  
21 parameters obtained with sideband-selective  $^1\text{H}\{^{195}\text{Pt}\}$  TONE D-HMQC-4 for **1** ( $\Omega = 8816$  ppm,  
22  $\kappa = -0.95$ ) are in close agreement with the known values ( $\Omega = 8975$  ppm,  $\kappa = -0.96$ ).<sup>60, 71</sup> Analysis  
23  
24 of the sideband-selective PE RESPDOR data set yields  $\Omega = 8687$  ppm and  $\kappa = -0.7$ , again in good  
25  
26 agreement with the established CSA tensor parameters (Figure S11C).  
27  
28  
29  
30  
31  
32

33  $^1\text{H}\{^{195}\text{Pt}\}$  sideband-selective NMR experiments were also applied to **2**, which has not  
34 previously been analyzed by  $^{195}\text{Pt}$  solid-state NMR. The 1D  $^1\text{H}$  solid-state NMR spectrum of **2**  
35 showed two signals at 1.9 and 6.3 ppm, corresponding to the methyl and CH hydrogen atoms of  
36 the acetylacetonate ligands, respectively (Figure 3B). A standard 1D  $^1\text{H}\{^{195}\text{Pt}\}$  TONE D-HMQC-  
37  
38 **2** spectrum showing both  $^1\text{H}$  NMR signals can be obtained in a few minutes (Figure 3B), despite  
39  
40 the long  $^1\text{H}$   $T_1$  (36 and 50 s for the methyl and methine  $^1\text{H}$ , respectively) and small  $^1\text{H}$ - $^{195}\text{Pt}$   
41  
42 heteronuclear dipolar couplings of ca. 300 Hz (see  $^1\text{H}\{^{195}\text{Pt}\}$  SHAP S-REDOR experiments<sup>66, 74</sup>  
43  
44 in Figure S13A). Rotor-synchronized 2D TONE D-HMQC-4 experiments were performed with  
45  
46 MAS frequencies of 50 and 52 kHz to measure the  $^{195}\text{Pt}$  isotropic chemical shift of **2** (Figure  
47  
48 S13B). Notably, two  $^{195}\text{Pt}$  signals at  $-360$  and  $-385$  ppm were observed, suggesting that the sample  
49  
50  
51  
52  
53  
54  
55  
56  
57  
58  
59  
60

1  
2  
3 studied here contains two crystallographically inequivalent sites, in disagreement with the  
4 currently known crystal structure of **2**.<sup>91</sup> A <sup>13</sup>C CPMAS spectrum of **2** also shows more peaks than  
5 expected, yet the experimental PXRD pattern closely matches that predicted from the 200 K X-  
6 ray structure (Figure S13). Hence, we conclude that the sample of **2** studied here was phase pure,  
7 but that the structure at room temperature may be slightly different from the reported 200 K single-  
8 crystal X-ray structure. A wide-line <sup>1</sup>H{<sup>195</sup>Pt} D-HMQC experiment on **2** takes 45 hours and it  
9 suffers from an incomplete excitation because of the large CSA (Figure S13C). The  $\Omega$  was  
10 estimated to be 11800 ppm (Figure S13D, Note S2), in good agreement with a previous estimate  
11 of 10000 ppm from solution <sup>195</sup>Pt NMR relaxation experiments.<sup>92</sup> On the other hand, with  
12 sideband-selective TONE D-HMQC-4 and PE RESPDOR experiments, <sup>195</sup>Pt NMR spectra were  
13 obtained in only 15 and 13 hours, respectively (Figure 3). Fits of the <sup>195</sup>Pt NMR spectra obtained  
14 with TONE D-HMQC-4 or PE RESPDOR yielded a  $\kappa$  of  $-0.7$  and similar  $\Omega$  values of 12682 ppm  
15 or 12521 ppm (Figure S14), which agree with the parameters determined from the MAS <sup>195</sup>Pt NMR  
16 spectrum extracted from the <sup>1</sup>H{<sup>195</sup>Pt} D-HMQC experiment (Figure S13D). Resolving the two  
17 CSA patterns for the two platinum sites of **2** is not possible under our experimental conditions  
18 because of their similar isotropic shifts (ca. 15 ppm and 2150 Hz isotropic shift difference).  
19  
20  
21  
22  
23  
24  
25  
26  
27  
28  
29  
30  
31  
32  
33  
34  
35  
36  
37  
38  
39

40 In summary, the sideband-selective <sup>1</sup>H{<sup>195</sup>Pt} TONE D-HMQC and PE RESPDOR  
41 experiments were performed with unprecedented sensitivity: the entire <sup>195</sup>Pt MAS NMR spectrum  
42 of cisplatin was obtained in only 1 hour with TONE D-HMQC-4 and 24 minutes with PE  
43 RESPDOR. For Pt(acac)<sub>2</sub> the <sup>195</sup>Pt MAS NMR spectrum was obtained within 15 hours, despite the  
44 unfavorable NMR properties of **2**. Given the high signal to noise ratios observed with cisplatin  
45 (Figure S15), preliminary <sup>195</sup>Pt MAS NMR spectra can typically be obtained in a few minutes for  
46 most pure compounds. With these remarkable first results on molecular compounds, sideband-  
47  
48  
49  
50  
51  
52  
53  
54  
55  
56  
57  
58  
59  
60

selective  $^1\text{H}\{^{195}\text{Pt}\}$  solid-state NMR experiments were then applied to examine silica-supported platinum compounds.

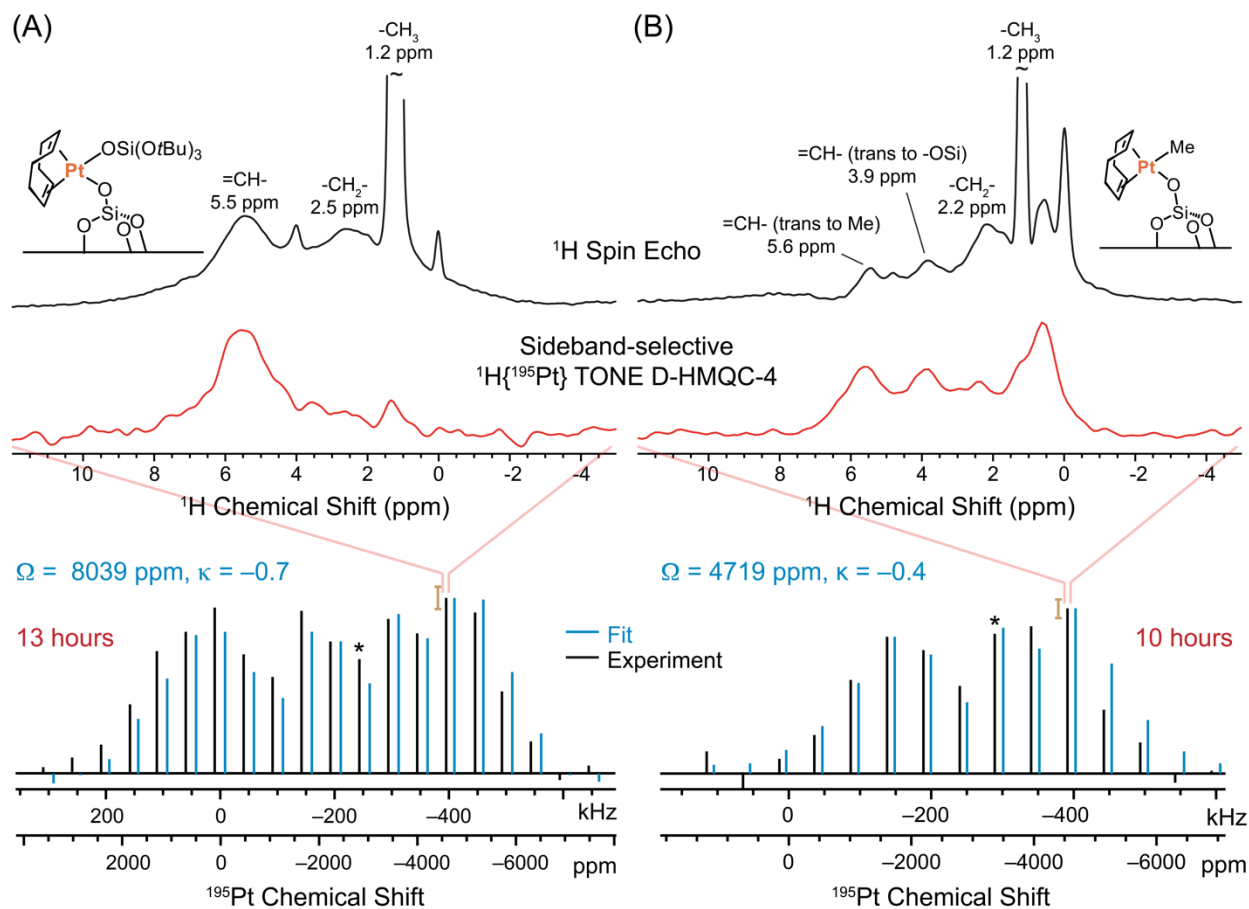


**Figure 4.**  $^{195}\text{Pt}$  sideband-selective NMR experiments with silica-supported Pt compounds (A) **3**/ $\text{SiO}_2$  and (B) **4**/ $\text{SiO}_2$ . (top) 1D  $^1\text{H}$  spin echo NMR spectra, (middle) sideband-selective  $^1\text{H}\{^{195}\text{Pt}\}$  TONE D-HMQC-4 spectra at the indicated  $^{195}\text{Pt}$  offset (corresponding to the most intense sidebands). (bottom, black trace)  $^1\text{H}\{^{195}\text{Pt}\}$  sideband-selective TONE D-HMQC-4 spectra of (A) **3**/ $\text{SiO}_2$  and (B) **4**/ $\text{SiO}_2$ , obtained from the intensities of the CH  $^1\text{H}$  NMR signal at ca. 5.5 ppm and the CH<sub>3</sub>  $^1\text{H}$  NMR signal at 1.2 ppm, respectively. (blue trace) SIMPSON simulations with TONE D-HMQC-2 using  $^{195}\text{Pt}$  (A)  $\Omega = 8039$  ppm,  $\kappa = -0.7$  and (B)  $\Omega = 4719$  ppm,  $\kappa = -0.4$ , which correspond to the CSA tensors parameters that give the lowest RMSD. The error bar accounting for SNR is shown for the most intense sideband. Intense *t*-butoxide methyl signals were truncated in the  $^1\text{H}$  spin echo NMR spectra. All experiments were performed with a 50 kHz MAS frequency.

*MAS  $^{195}\text{Pt}$  Solid-State NMR of Surface Species.* In order to investigate materials used in heterogeneous catalysis, we first measured the  $^{195}\text{Pt}$  CSA of a model single-site compound prepared by grafting **3** [(COD)Pt(OSi(O*t*Bu)<sub>3</sub>)] on partially dehydroxylated silica<sup>12, 49, 93</sup> which



1  
2  
3 yields (**3/SiO<sub>2</sub>**) with a surface Pt loading of 3.73 wt.% (ca. 1 Pt/nm<sup>2</sup>). Recently, we determined the  
4  
5 CS tensor parameters of **3/SiO<sub>2</sub>** ( $\delta_{\text{iso}} = -2819$  ppm,  $\Omega = 8412$  ppm,  $\kappa = -0.77$ ) using a combination  
6  
7 of DNP-SENS <sup>1</sup>H→<sup>195</sup>Pt BRAIN-CP WCPMG and isotropic fast MAS <sup>1</sup>H-<sup>195</sup>Pt TONE D-HMQC  
8  
9 experiments that required approximately five days and one day of spectrometer time,  
10  
11 respectively.<sup>66</sup> As we showed previously, the <sup>195</sup>Pt isotropic peak and sidebands of the grafted  
12  
13 compound are broad (ca. 8-10 kHz full width at half maximum) because of an inhomogeneous  
14  
15 distribution of isotropic shifts likely related to slightly different local environments, a result from  
16  
17 the amorphous character of silica.<sup>66</sup> To enable efficient excitation/saturation in the sideband-  
18  
19 selective experiments, 40  $\mu$ s excitation pulses with an optimal rf field of 16 kHz were used (Table  
20  
21 S1, Figure S3-S4). The sideband-selective TONE D-HMQC-4 experiment yielded the MAS <sup>195</sup>Pt  
22  
23 CSA pattern within 13 hours that could be fitted to  $\Omega = 8039$  ppm,  $\kappa = -0.7$ , consistent with the  
24  
25 reported values mentioned above (Figure 4A and Figure S16-S17). Although PE RESPDOR  
26  
27 showed only a maximum dephasing of 5% (corresponding to an estimated error of ca. 20% of the  
28  
29 dephasing difference signal intensities), a <sup>195</sup>Pt NMR spectrum was obtained in only 3.3 hours and  
30  
31 fits of this spectrum gave  $\Omega = 7876$  ppm,  $\kappa = -0.8$  (Figure S17). The significant savings in time  
32  
33 (few hours) compared to our previous report (6 days),<sup>66</sup> demonstrates the high sensitivity of the  
34  
35 sideband-selective experiments for measurement of <sup>195</sup>Pt NMR spectra.  
36  
37  
38  
39  
40  
41  
42

43 To probe if the sideband-selective experiments are suitable to detect differences in the  
44  
45 ligand environment of supported compounds, we obtained <sup>195</sup>Pt NMR spectra of  
46  
47 [(COD)PtMe]/SiO<sub>2</sub> (**4/SiO<sub>2</sub>**) that has a surface Pt loading of 4.96 wt.%. In **4/SiO<sub>2</sub>**, the -OSi(O*t*Bu)<sub>3</sub>  
48  
49 ligand of **3/SiO<sub>2</sub>** is replaced with a methyl ligand. Consequently, in **4/SiO<sub>2</sub>** the two sets of olefinic  
50  
51 protons in the COD ligand become inequivalent; the CH protons *trans* to the methyl and -OSi  
52  
53 groups appear at 5.6 and 3.9 ppm, respectively, in close accordance with the solution <sup>1</sup>H NMR  
54  
55  
56  
57  
58  
59  
60

1  
2  
3 spectrum of **4** ( $\delta_{\text{iso}} = 5.90$  and  $3.56$  ppm, Figure S18).<sup>12</sup> As a result, the signal intensities of the  
4 olefinic protons is halved in comparison to **3/SiO<sub>2</sub>** which will decrease the overall indirect  
5 detection sensitivity. However, the methyl group protons at  $1.2$  ppm are also in close proximity to  
6 the Pt center and can also be used as spy nuclei for the indirect detection experiments. Indeed, all  
7 of these <sup>1</sup>H NMR signals are clearly observed in rotor-synchronized 1D and 2D <sup>1</sup>H{<sup>195</sup>Pt} TONE  
8 D-HMQC-2 spectra (Figure 4B, Figure S19), indicating that COD and methyl ligands remain  
9 coordinated to Pt after grafting on silica. For **4/SiO<sub>2</sub>**  $\delta_{\text{iso}}$  was determined to be  $-3327$  ppm from  
10 the rotor-synchronized 2D <sup>1</sup>H{<sup>195</sup>Pt} TONE D-HMQC-2 spectra (Figure S19). A single 1D  
11 sideband-selective <sup>1</sup>H{<sup>195</sup>Pt} TONE D-HMQC-4 spectrum can be acquired in only 40 minutes  
12 with a SNR of 20 at the most intense sideband. Consequently, the entire <sup>195</sup>Pt MAS NMR spectrum  
13 of **4/SiO<sub>2</sub>** was obtained in only 10 hours (Figure 4B). Least-squares fitting of the resulting pattern  
14 with SIMPSON simulations provides  $\Omega = 4719$  ppm,  $\kappa = -0.7$  (Figure S20), which illustrates a  
15 significant lowering of the span in comparison to **3/SiO<sub>2</sub>**. These results demonstrate that the new  
16 solid-state NMR experiments are well suited to capture differences in Pt environments of surface  
17 species.  
18  
19  
20  
21  
22  
23  
24  
25  
26  
27  
28  
29  
30  
31  
32  
33  
34  
35  
36  
37  
38  
39  
40  
41  
42  
43  
44  
45  
46  
47  
48  
49  
50  
51  
52  
53  
54  
55  
56  
57  
58  
59  
60

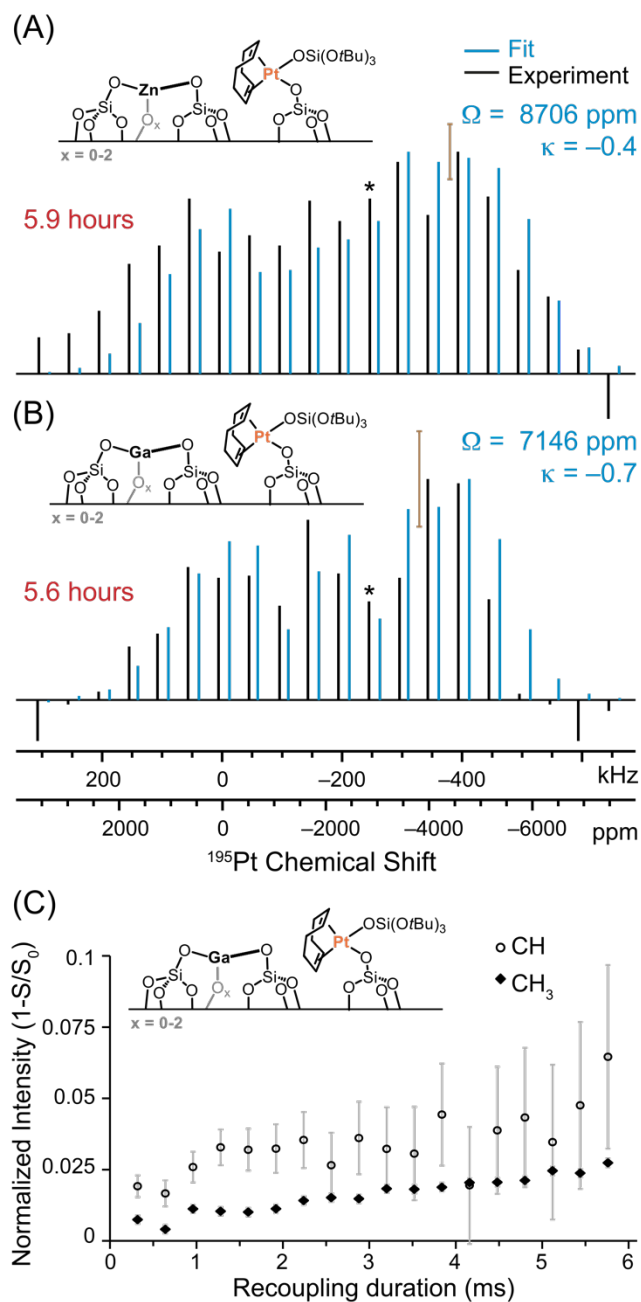


**Figure 5.** Sideband-selective  $^1\text{H}\{^{195}\text{Pt}\}$  PE RESPDOR experiments on single-site Pt compounds (A) **3\_Zn/SiO<sub>2</sub>** and (B) **3\_Ga/SiO<sub>2</sub>**. (black) Experimental patterns and (blue) SIMPSON simulations performed using the indicated CS tensor parameters. A maximum experimental signal dephasing of (A) 6.4% and (B) 3.7% was observed. Error bars are shown for the most intense sidebands. (C)  $^1\text{H}\{^{71}\text{Ga}\}$  PE RESPDOR build-up curves: plot showing normalized dephasing difference signal intensity ( $1-S/S_0$ ) as a function of dipolar recoupling duration for (circles) CH and (diamonds) CH<sub>3</sub> groups in the grafted [(COD)Pt(OSi(OtBu)<sub>3</sub>)] complex.

In order to probe the sensitivity of these newly developed NMR experiments to modifications on the surface, we investigated the surface species of [(COD)Pt(OSi(OtBu)<sub>3</sub>)<sub>2</sub>]

1  
2  
3 grafted on silica doped with different Lewis acids, namely Zn(II) and Ga(III), in order to probe the  
4 local environment around Pt and determine if there are any interactions of Pt with the adjacent  
5 Lewis acid sites. These systems, denoted **3\_Zn/SiO<sub>2</sub>** and **3\_Ga/SiO<sub>2</sub>**, were chosen because they  
6 are used as precursors to prepare highly active mixed-metal nanoparticle catalysts for the non-  
7 oxidative propane dehydrogenation.<sup>13, 15-16</sup> The 1D <sup>1</sup>H NMR spectra of both compounds clearly  
8 show signals corresponding to CH<sub>3</sub> (ca. 1.2 ppm), CH<sub>2</sub> (ca. 2.2 ppm) and the olefinic CH (ca. 5.6  
9 ppm) protons (Figure S21), in good agreement with the chemical shift assignments of **3/SiO<sub>2</sub>**.<sup>66</sup>  
10 The ligand structure was further confirmed by 2D <sup>1</sup>H single quantum-double quantum (SQ-DQ)  
11 correlation spectroscopy, and <sup>13</sup>C and <sup>29</sup>Si DNP-SENS (Figure S21-S23). Rotor-synchronized 2D  
12 <sup>1</sup>H{<sup>195</sup>Pt} TONE D-HMQC spectra were used to measure the isotropic <sup>195</sup>Pt chemical shifts of –  
13 2844 and –2828 ppm for **3\_Zn/SiO<sub>2</sub>** and **3\_Ga/SiO<sub>2</sub>**, respectively (Figure S24). These isotropic  
14 shift values are entirely consistent with a similar Pt local environment as found in **3/SiO<sub>2</sub>** (<sup>195</sup>Pt  
15  $\delta_{\text{iso}} = -2819$  ppm).  
16  
17  
18  
19  
20  
21  
22  
23  
24  
25  
26  
27  
28  
29  
30  
31  
32

33 Figure 5A and 5B shows comparisons between experimental sideband patterns obtained  
34 with <sup>1</sup>H{<sup>195</sup>Pt} PE RESPDOR and corresponding SIMPSON simulations using the best fit <sup>195</sup>Pt  
35 CS tensor parameters. Sideband-selective <sup>1</sup>H{<sup>195</sup>Pt} PE RESPDOR was used to measure the <sup>195</sup>Pt  
36 MAS NMR spectra of **3\_Zn/SiO<sub>2</sub>** and **3\_Ga/SiO<sub>2</sub>** because it provided better sensitivity than TONE  
37 D-HMQC. We obtained  $\Omega = 8706$  ppm and  $\kappa = -0.4$  for **3\_Zn/SiO<sub>2</sub>** and  $\Omega = 7146$  ppm,  $\kappa = -0.7$   
38 for **3\_Ga/SiO<sub>2</sub>**, from least-squares fitting (Figure S25). Notably, the <sup>195</sup>Pt NMR spectra obtained  
39 with the sideband-selective experiments are clearly superior to those obtained with DNP-SENS  
40 <sup>1</sup>H→<sup>195</sup>Pt BRAIN-CP-WCPMG<sup>62</sup> NMR experiments, which provided only partial excitation of  
41 the <sup>195</sup>Pt shielding patterns, with greatly reduced intensity at the high-frequency side of the pattern  
42  
43  
44  
45  
46  
47  
48  
49  
50  
51  
52  
53  
54  
55  
56  
57  
58  
59  
60

1  
2  
3 (Figure S26). Note that similar distortions of intensity were previously seen in the  $^1\text{H} \rightarrow ^{195}\text{Pt}$   
4 BRAIN-CP-WCPMG spectrum of  $\mathbf{3}/\text{SiO}_2$ .<sup>66</sup>  
5  
6

7  
8 Clearly, the structure of the grafted single-site  $[(\text{COD})\text{Pt}(\text{OSi}(\text{O}t\text{Bu})_3)]$  species in  
9  
10  $\mathbf{3\_Zn}/\text{SiO}_2$  is similar to  $\mathbf{3}/\text{SiO}_2$ . In case of  $\mathbf{3\_Ga}/\text{SiO}_2$ , the observed  $^{195}\text{Pt}$  sideband manifold  
11  
12 indicates a span that is lower than that of  $\mathbf{3}/\text{SiO}_2$  by ca. 1250 ppm, which could indicate differing  
13  
14 interactions between the grafted Pt compounds and the co-grafted  $\text{Ga}^{3+}$  and  $\text{Zn}^{2+}$  ions, that in turn  
15  
16 suggests slight average differences in the conformation and electronic structure. Note that the  
17  
18 reduction in span of  $\mathbf{3\_Ga}/\text{SiO}_2$  could also be partially attributed to the error in intensities due to  
19  
20 a low PE RESPDOR dephasing of ca. 3.7%. To confirm the proximity of the co-grafted Pt complex  
21  
22 and the  $\text{Ga}^{3+}$  ions, we performed  $^1\text{H}\{^{71}\text{Ga}\}$  PE RESPDOR experiments which show dephasing of  
23  
24 the olefinic CH and the methyl groups of the siloxide ligand (Figure 5C). The slow build-up of the  
25  
26  $^1\text{H}\{^{71}\text{Ga}\}$  PE RESPDOR curve is consistent with  $^1\text{H}$ - $^{71}\text{Ga}$  inter-nuclear distances on the order of  
27  
28 several angstroms. Similar RESPDOR experiments could not be performed on  $\mathbf{3\_Zn}/\text{SiO}_2$  due to  
29  
30 the low  $^{67}\text{Zn}$  natural abundance of 4.1%.  
31  
32  
33  
34  
35  
36  
37  
38  
39  
40  
41  
42  
43  
44  
45  
46  
47  
48  
49  
50  
51  
52  
53  
54  
55  
56  
57  
58  
59  
60

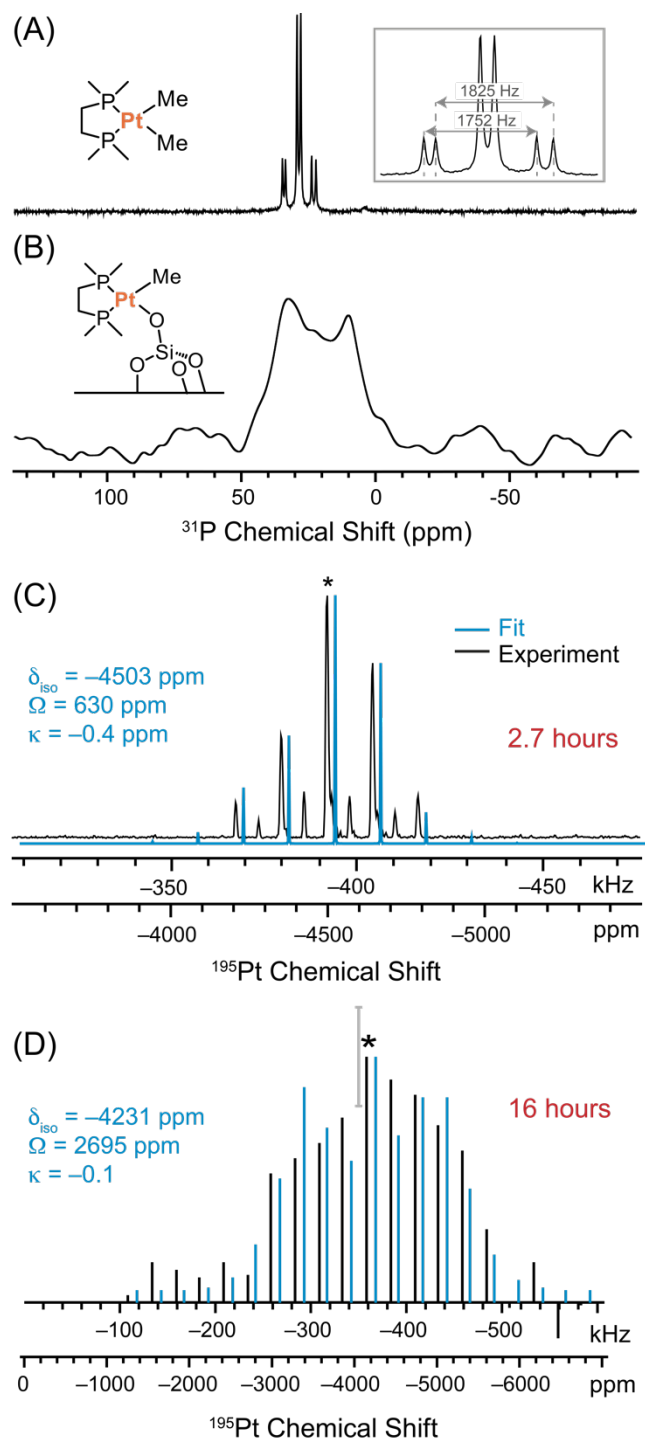


**Figure 6.**  $^{31}\text{P}\{^{195}\text{Pt}\}$  NMR experiments on compounds **5** and **5/SiO<sub>2</sub>**.  $^1\text{H}\rightarrow^{31}\text{P}$  CP-MAS spectra of (A) **5** and (B) **5/SiO<sub>2</sub>** obtained with a 25 kHz MAS frequency. (C) 1D  $^{195}\text{Pt}$  projection from a 2D  $^{31}\text{P}\{^{195}\text{Pt}\}$  CP constant time  $J$ -HMQC spectrum of **5** acquired with a 12.5 kHz MAS frequency. (D)  $^{195}\text{Pt}$  CSA pattern of **5/SiO<sub>2</sub>** acquired with a sideband-selective  $^1\text{H}\text{-}^{31}\text{P}\{^{195}\text{Pt}\}$  CP  $J$ -resolved pulse sequence using CPMG detection and a 25 kHz MAS frequency.

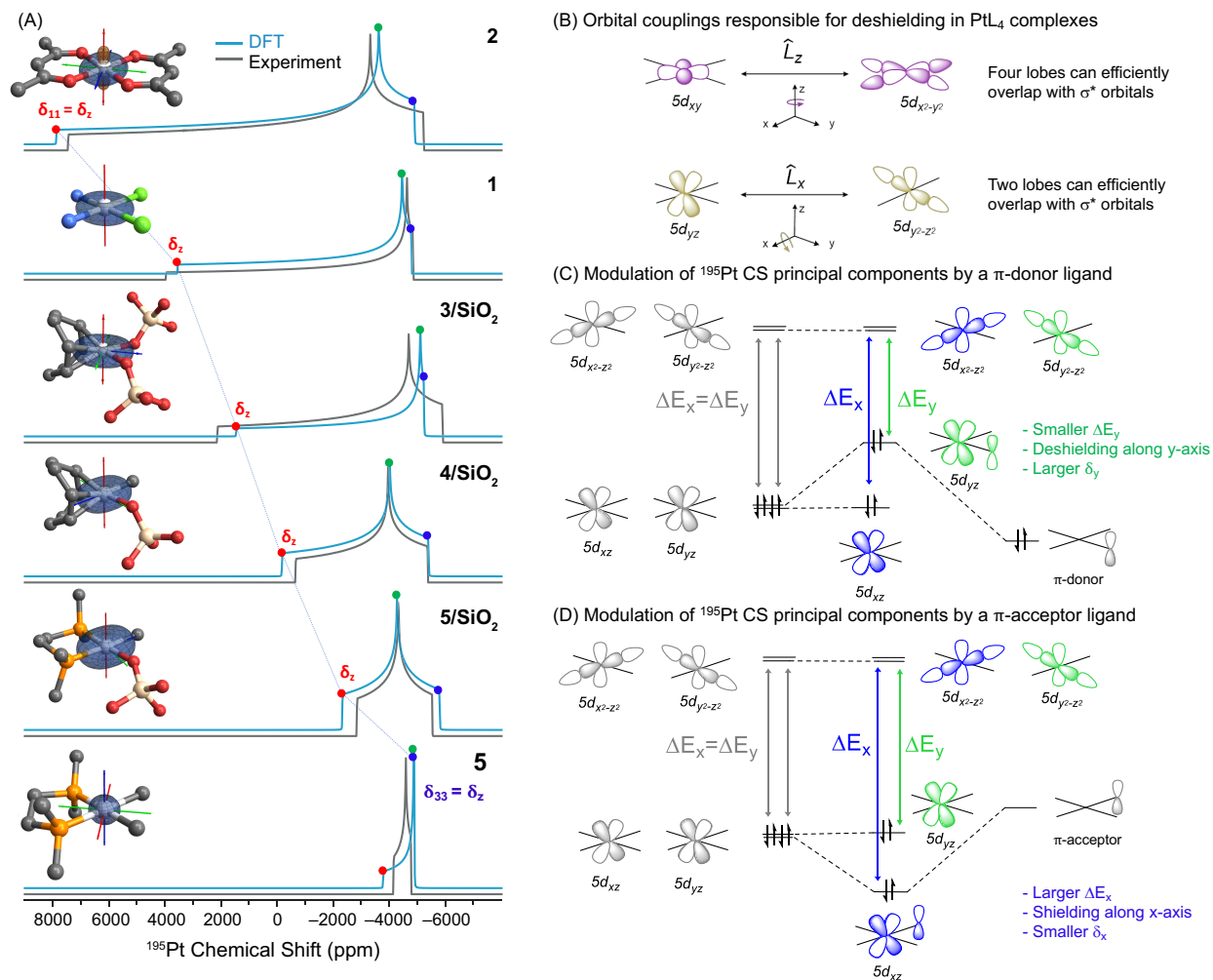
$^{31}\text{P}\{^{195}\text{Pt}\}$  *J*-HMQC and *J*-Resolved NMR Experiments. While  $^1\text{H}$  spins near  $^{195}\text{Pt}$  were used to indirectly observe  $^{195}\text{Pt}$  CSA patterns and determine the local structure of single-site Pt compounds, many catalysts can contain alternative ligands, such as phosphines.  $^{31}\text{P}$  can also serve as a spy nucleus for sideband-selective experiments as it offers good NMR sensitivity. We demonstrate this approach with [(DMPE)PtMe<sub>2</sub>] (**5**) and the corresponding supported compound **5/SiO<sub>2</sub>** (Figure 1) using *J*-based  $^1\text{H}$ - $^{31}\text{P}\{^{195}\text{Pt}\}$  solid-state NMR experiments performed with a triple-resonance 2.5 mm HXY probe and MAS frequencies of 12.5 and 25 kHz, respectively.

Figure 6A shows a  $^1\text{H}\rightarrow^{31}\text{P}$  CP-MAS spectrum of **5**, which can be obtained within a few minutes. Two  $^{31}\text{P}$  sites are observed at 29.1 ppm and 30.4 ppm with  $^1J_{\text{P-Pt}}$  values of 1825 and 1750 Hz, respectively. Both the chemical shifts and  $^1J_{\text{P-Pt}}$  values agree closely with previous solution NMR measurements.<sup>94</sup> Note that small variations in bond angles/lengths in the solid-state can create inequivalence and cause two  $^{31}\text{P}$  NMR signals to be observed instead of one. A  $^{31}\text{P}\{^{195}\text{Pt}\}$  constant-time *J*-HMQC experiment was then performed on **5** (Figure S27A). The constant-time format of the HMQC experiment enables arbitrary and large  $F_1$  spectral widths necessary for the indirect detection of  $^{195}\text{Pt}$  spinning sideband manifolds.<sup>71</sup> The resulting  $^{195}\text{Pt}$  NMR spectrum was fit to CS tensor parameters of  $\delta_{\text{iso}} = -4503$  ppm,  $\Omega = 630$  ppm and  $\kappa = -0.4$  (Figure 6C).

The  $^{31}\text{P}$  CP-MAS spectrum of **5/SiO<sub>2</sub>** has a low SNR (ca. 9 after 3.5 hours of acquisition) because of the low Pt surface loading of 4.4 wt % and signal broadening due to surface disorder (Figure 6B). Additionally, the  $^{31}\text{P}$  NMR spectrum of **5/SiO<sub>2</sub>** shows two characteristic features at 35 and 10 ppm, consistent with the inequivalence of the two phosphines in the grafted species: one is *trans* to a methyl (35 ppm), while the other is *trans* to a siloxide group (10 ppm). CPMG detection was used to accelerate all  $^{31}\text{P}\{^{195}\text{Pt}\}$  solid-state NMR experiments on **5/SiO<sub>2</sub>**. Due to low sensitivity, it was not possible to perform a  $^{31}\text{P}\{^{195}\text{Pt}\}$  wide-line *J*-HMQC experiment on **5/SiO<sub>2</sub>**.

1  
2  
3 However, a rotor-synchronized  $^{31}\text{P}\{^{195}\text{Pt}\}$   $J$ -HMQC spectrum showed that the  $^{195}\text{Pt}$  isotropic  
4 chemical shift of **5/SiO<sub>2</sub>** was  $-4231$  ppm (Figure S27B, Figure S28). The  $^{195}\text{Pt}$  CSA of **5/SiO<sub>2</sub>** was  
5 then measured using a  $^{31}\text{P}\{^{195}\text{Pt}\}$  CP  $J$ -resolved (heteronuclear spin echo) experiment with  $40\ \mu\text{s}$   
6  $^{195}\text{Pt}$  sideband-selective saturation pulses at  $22$  kHz rf field (Figure 6D). The dephasing observed  
7 for CPMG spikelets at  $36$  and  $29$  ppm was averaged to improve the SNR (Figure S29). With this  
8 approach, the sideband manifold could be obtained in only  $16$  hours. Least-squares fitting of the  
9 sideband manifold yields  $\Omega = 2695$  ppm and  $\kappa = -0.1$  (Figure 6D, Figure S30). Interestingly, the  
10 values of  $\delta_{\text{iso}}$  for **5** and **5/SiO<sub>2</sub>** only differ by  $272$  ppm, a small difference with respect to the large  
11 chemical shift range of  $^{195}\text{Pt}$ . However, the value of  $\Omega$  for **5/SiO<sub>2</sub>** is considerably larger than that  
12 measured for **5** ( $2695$  vs  $630$  ppm), illustrating the importance of measuring CSA to probe the  
13 changes in the local Pt coordination environment upon grafting. The origin of the large difference  
14 in  $^{195}\text{Pt}$  CSA is further discussed below. In conclusion, sideband-selective  $^{31}\text{P}\{^{195}\text{Pt}\}$   $J$ -resolved  
15 experiments enabled acquisition of the  $^{195}\text{Pt}$  NMR spectrum of **5/SiO<sub>2</sub>** in only  $16$  hours,  
16 demonstrating that NMR-active nuclei other than  $^1\text{H}$  can be used for indirect detection of  $^{195}\text{Pt}$   
17 NMR spectra.  
18  
19  
20  
21  
22  
23  
24  
25  
26  
27  
28  
29  
30  
31  
32  
33  
34  
35  
36  
37  
38  
39  
40  
41  
42  
43  
44  
45  
46  
47  
48  
49  
50  
51  
52  
53  
54  
55  
56  
57  
58  
59  
60





**Figure 7.** (A) Simulated static  $^{195}\text{Pt}$  CSA parameters obtained using parameters from (black traces) sideband-selective NMR experiments and (blue traces) ZORA DFT calculations. The DFT optimized structures and the corresponding 3D representations of the calculated shielding tensors are shown for each compound. (B) Orbital couplings responsible for paramagnetic deshielding in square planar  $\text{PtL}_4$  complexes. Modulation of orbital energies and Pt CS principal components in the plane by (C) a  $\pi$ -donor and (D) a  $\pi$ -acceptor ligand. In (A), blue and orange lobes indicate positive and negative shielding, respectively. The CSA principal components color code is:  $\delta_{11} > \delta_{22} > \delta_{33}$ . Plots of the shielding tensors are scaled to 0.002 pm/ppm. A summary of  $^{195}\text{Pt}$  CSA parameters from different methods are provided in the Supporting Information in Table S2. NMR calculations of the supported species were performed using with *t*-butoxy siloxide groups in place of the silica surface. Hydrogen atoms are omitted for clarity. For the same reason, only the  $\text{SiO}_4$  unit of the siloxide ligands is shown.

*DFT Calculations of  $^{195}\text{Pt}$  CS Tensors.* Finally, we used spin-orbit ZORA DFT calculations to compute the  $^{195}\text{Pt}$  CS tensor parameters of the molecular and supported Pt-species studied.<sup>95-96</sup> The differences in CSA parameters can be related to differences in the coordination environments using simple and powerful orbital models. Modern computational chemistry packages allow

1  
2  
3 accurate prediction of NMR properties, including  $^{195}\text{Pt}$  chemical shifts,<sup>58-59, 97</sup> which is useful for  
4 structure determination by NMR crystallography protocols.<sup>55, 98-99</sup> As demonstrated by Ziegler, the  
5 origin of the  $^{195}\text{Pt}$  CSA can be traced back to electronic structure.<sup>100</sup> Autschbach subsequently  
6 demonstrated a localized molecular orbital analysis of  $^{195}\text{Pt}$  CS tensors that provides a clear link  
7 between the energy and symmetry of orbitals in square planar Pt compounds and the observed CS  
8 tensor parameters:<sup>55, 59</sup> the deshielding for the CS component along the  $z$  direction of the molecular  
9 frame (denoted  $\delta_z$ ), originate from the coupling of the high-lying, filled  $d_{xy}$  orbital with the  
10 antibonding  $\sigma^*(\text{Pt-L})$  orbital by the  $\hat{L}_z$  operator and, to a minor extent, from the filled  $d_{xz}$  and  $d_{yz}$   
11 Pt orbitals coupling with the specific  $\sigma^*(\text{Pt-L})$  along the  $y$  or  $x$  axis, by  $\hat{L}_y$  and  $\hat{L}_x$  respectively  
12 (Figure 7B, details in experimental section below).

13  
14  
15  
16  
17  
18  
19  
20  
21  
22  
23  
24  
25  
26 Standard gas-phase DFT calculations using the Gaussian09 program<sup>101</sup> were used to  
27 optimize atomic coordinates. Then, ZORA DFT calculations as implemented in the ADF  
28 program<sup>102</sup> were used to calculate  $^{195}\text{Pt}$  CSA principal components ( $\delta_{11} > \delta_{22} > \delta_{33}$ ) (for additional  
29 details, see the experimental section). The computed and experimental values of CSA are in good  
30 agreement, thus validating the computational approach (see Figure 7A and Table S2).

31  
32  
33  
34  
35  
36  
37  
38 In all but one case,  $\delta_{11}$ , the most deshielded component, lies perpendicular to the plane,  
39 along the natural  $z$ -axis of these square planar compounds ( $\delta_{11} = \delta_z$ ). The exception is for  
40 compound **5**, where  $\delta_{33}$  is aligned with the molecular  $z$ -axis. Across the series of square planar  
41 compounds studied here, the value of  $\delta_z$  varies from +7873 to -4885 ppm, while the other  
42 components in the plane ( $\delta_x/\delta_y$ ), varies only within ca. 2000 ppm. Note also that small changes in  
43 geometry significantly affect  $^{195}\text{Pt}$  CS tensor parameters (Figure S31).

44  
45  
46  
47  
48  
49  
50  
51  
52  
53 The (de)shielding across the series of Pt-species studied here is clearly affected by the  
54 energy of  $\sigma^*(\text{Pt-L})$  orbitals, which is determined by the  $\sigma$ -donating properties of the corresponding  
55

1  
2  
3 L ligands (Note S3). Thus, it may not be so surprising that changes in the coordination sphere of  
4  
5 Pt<sup>II</sup>L<sub>4</sub> compounds dramatically affect the  $\delta_z$  component, which varies from +7873 (**2**) to -4885  
6  
7 ppm (**5**) upon going from oxygen to carbon-based ligands. As discussed above, the compound **5**  
8  
9 presents the most shielded value for  $\delta_z$  that correspond to  $\delta_{33}$  and not  $\delta_{11}$  as for the other compounds  
10  
11 discussed here. Using the orbital-rotation model (Figure 7B, details in SI), one can readily justify  
12  
13 the much more shielded value for  $\delta_z$  in **5** which contains four strong  $\sigma$ -donor ligands bound to Pt  
14  
15 (two methyl and two phosphine), hence the increase of  $\sigma^*(\text{Pt-L})$  orbital energies and high shielding  
16  
17 of the Pt nucleus. At the opposite end, the compound **2** with acac ligands has four weak  $\sigma$ -donor  
18  
19 oxygen atoms bound to Pt, leading to a lower  $\sigma^*(\text{Pt-L})$  orbital energy and the more deshielding  $\delta_z$   
20  
21 (larger positive value). Overall, the strength of the  $\sigma$ -donating ligands drives the value of  $\delta_z$  and  
22  
23 determine the overall anisotropy and isotropic CS.  
24  
25  
26  
27  
28

29 The sensitivity of the CS tensor parameters to the types of coordinated ligands explains  
30  
31 why **5** and the supported **5/SiO<sub>2</sub>** have significantly different spans (Figure 7A). The replacement  
32  
33 of one Pt-methyl bond in **5** by a Pt-siloxide bond in **5/SiO<sub>2</sub>** upon grafting, leads to a more  
34  
35 deshielded  $\delta_z$  component, as a result of the lower  $\sigma$ -donating properties of the siloxide ligand. This  
36  
37 analysis also proves suitable to understand the differences in spans among supported Pt sites. For  
38  
39 the supported species **3/SiO<sub>2</sub>** and **4/SiO<sub>2</sub>** the latter has a more shielded  $\delta_z$  component, resulting  
40  
41 from the presence of a methyl group, a strong  $\sigma$ -donor ligand. A remarkable difference in  $\delta_z$  can  
42  
43 also be observed between **4/SiO<sub>2</sub>** and **5/SiO<sub>2</sub>**, where a more shielded  $\delta_z$  in the latter can be related  
44  
45 to the stronger  $\sigma$ -donating properties of DMPE with respect to the COD ligand.  
46  
47  
48

49 Although CSA parameters in square planar Pt<sup>II</sup>L<sub>4</sub> complexes are mostly affected by  $\sigma$ -  
50  
51 interactions, the other principal components lying in the plane can be modulated through  $\pi$ -bonding  
52  
53 interactions. These effects are observed upon comparison of **3/SiO<sub>2</sub>** with the respective asymmetric  
54  
55  
56  
57  
58  
59  
60

1  
2  
3 complex **4/SiO<sub>2</sub>**. While the symmetric molecular model for **3/SiO<sub>2</sub>** (having two siloxide ligands)  
4 has an axially symmetric CS tensor ( $\delta_{22} \approx \delta_{33} \approx -5150$  ppm), the asymmetric system **4/SiO<sub>2</sub>**, with  
5 both a siloxide (weak  $\pi$ -donor) and a methyl ligand (mostly  $\sigma$ -donor) has  $\delta_{22} (-4021 \text{ ppm}) \gg \delta_{33}$   
6  $(-5400 \text{ ppm})$ . In **4/SiO<sub>2</sub>**, the most shielded component  $\delta_{33}$  is aligned with the Pt-methyl bond, while  
7  $\delta_{22}$  is aligned with the Pt-siloxide bond. Specifically, the presence of a  $\pi$ -donor ligand causes an  
8 increase in energy of the overlapping filled Pt  $5d_{yz}$  orbital through an antibonding interaction,  
9 which ultimately results in an increased energy of the  $5d_{yz}$  orbital that allows for a more efficient  
10 coupling with  $\sigma^*(\text{Pt-L})$ , hence the observed deshielding in the direction of the coupling (Figure  
11 7C). On the contrary, a  $\pi$ -acceptor ligand can interact with the filled Pt  $5d_{yz}$  orbital, stabilising it,  
12 and resulting in a less efficient orbital coupling due to increase in energy difference with the  
13 antibonding  $\sigma^*(\text{Pt-L})$  (Figure 7D). When combined, these orbital interactions lead to the observed  
14 effects in CSA of the asymmetric system **4/SiO<sub>2</sub>**; analogous observations can be made for **5/SiO<sub>2</sub>**.  
15 In summary, <sup>195</sup>Pt solid-state NMR spectra and CSA provide a signature of the metal sites, the  
16 types of ligands and the local symmetry of organometallic complexes and supported Pt species.  
17 Hence <sup>195</sup>Pt solid-state NMR spectroscopy is a powerful tool to characterize compounds and  
18 surface sites.  
19  
20  
21  
22  
23  
24  
25  
26  
27  
28  
29  
30  
31  
32  
33  
34  
35  
36  
37  
38  
39  
40  
41  
42

## 43 Conclusions

44 In conclusion, we have developed robust and expedient sideband-selective solid-state  
45 NMR methods to rapidly measure the <sup>195</sup>Pt NMR spectroscopic signatures of Pt-containing  
46 compounds and materials, including some having very large CSA such as Pt(acac)<sub>2</sub>. The sideband-  
47 selective NMR experiments offer an enormous time saving in comparison to state-of-the-art static  
48 DNP SENS experiments.<sup>66</sup> Additionally, the sideband-selective NMR methods can be performed  
49  
50  
51  
52  
53  
54  
55  
56  
57  
58  
59  
60

1  
2  
3 at room temperature and require only a few mg of material when performed with fast MAS probes  
4  
5 and small diameter rotors. These methods are based on low-power pulses that are one or more  
6  
7 rotor cycles in duration and provide sideband-selective excitation or saturation in fast MAS  
8  
9  $^1\text{H}\{^{195}\text{Pt}\}$  TONE D-HMQC-4 and PE RESPDOR experiments, thus allowing the reconstruction of  
10  
11 MAS  $^{195}\text{Pt}$  sideband intensities from a series of 1D NMR spectra. This approach was also extended  
12  
13 to sensitive spy nuclei such as  $^{31}\text{P}$  for indirect detection in sideband-selective  $^{31}\text{P}\{^{195}\text{Pt}\}$  *J*-resolved  
14  
15 experiments, thus showing that, even in the absence of  $^1\text{H}$  in the materials, other NMR active spy  
16  
17 nuclei can be utilized to obtain valuable molecular-level information on metal sites. Furthermore,  
18  
19 analysis of the CSA patterns down to the nature of the Pt-bonded ligands ( $\sigma$ -donor strength and  $\pi$ -  
20  
21 donating/accepting ability) provides an understanding of the trends in NMR parameters and also  
22  
23 demonstrates the potential of Pt NMR spectroscopy to distinguish subtle differences in the Pt-  
24  
25 coordination sphere. With this methodology in hand, we are currently exploring structure-  
26  
27 reactivity relationships in Pt-based single-atom catalysts, and are also investigating their  
28  
29 applications to other high *Z* spin-1/2 nuclei with moderate isotopic abundance that exhibit large  
30  
31 CSA. Finally, combining the sideband-selective NMR experiments with DNP should offer further  
32  
33 gains in sensitivity that will be needed to study dilute single-atom catalysts or enable the use of  
34  
35 nuclei such as natural abundance  $^{13}\text{C}$  as a spy-nucleus.  
36  
37  
38  
39  
40  
41  
42  
43  
44

## 45 **Experimental Section**

46  
47 **Synthesis of Materials.** All experiments were conducted inside an Argon filled MBraun  
48  
49 GloveBox or using standard Schlenk technique, using anhydrous reagents and distilled solvents,  
50  
51 unless indicated otherwise. All solvents were stored over 4 Å molecular sieves after being  
52  
53 transferred to a glove box. Silica ( $\text{SiO}_2$ , Aerosil 200®, 200 m<sup>2</sup> g<sup>-1</sup>) was calcined in air at 500°C  
54  
55  
56  
57  
58  
59  
60

1  
2  
3 before subsequent dehydroxylation at 700°C under high vacuum as reported in literature.<sup>10</sup> The  
4 resulting dehydroxylated silica is referred to as SiO<sub>2-700</sub>. Titration of the resulting SiO<sub>2-700</sub> using  
5 [Mg(CH<sub>2</sub>Ph)<sub>2</sub>(THF)<sub>2</sub>] purified *via* sublimation prior to use,<sup>103</sup> yielded an Si–OH density of 0.3  
6 mmol/g, corresponding to 0.9 accessible Si–OH groups per nm<sup>2</sup>. PtCl<sub>2</sub>(NH<sub>3</sub>)<sub>2</sub> (**1**, 99 % purity, Alfa  
7 Aesar) and Pt(acac)<sub>2</sub> (**2**, 98 % purity, Strem Chemicals) were used as received.  
8 [(COD)Pt(OSi(O<sup>t</sup>Bu)<sub>3</sub>)<sub>2</sub>] (**3**), [(COD)PtMe(OSi(O<sup>t</sup>Bu)<sub>3</sub>)] (**4**), [(DMPE)PtMe<sub>2</sub>] (**5**),  
9 [Zn(OSi(O<sup>t</sup>Bu)<sub>3</sub>)<sub>2</sub>]<sub>2</sub> and [Ga(THF)(OSi(O<sup>t</sup>Bu)<sub>3</sub>)<sub>3</sub>] molecular precursors were synthesized *via*  
10 literature procedures with minor modifications.<sup>12, 93, 104-106</sup> [(COD)Pt(OSi(O<sup>t</sup>Bu)<sub>3</sub>)]/SiO<sub>2</sub> (**3/SiO<sub>2</sub>**)  
11 was synthesized according to the previously described procedure.<sup>66</sup> The materials  
12 [(COD)Pt(OSi(O<sup>t</sup>Bu)<sub>3</sub>)]<sub>2</sub>Zn<sup>II</sup>/SiO<sub>2</sub> (**3\_Zn/SiO<sub>2</sub>**), [(COD)Pt(OSi(O<sup>t</sup>Bu)<sub>3</sub>)]<sub>2</sub>Ga<sup>III</sup>/SiO<sub>2</sub>  
13 (**3\_Ga/SiO<sub>2</sub>**) and [(COD)PtMe]/SiO<sub>2-700</sub> (**4/SiO<sub>2</sub>**) were synthesized following adapted literature  
14 procedures.<sup>12-13, 15</sup>

15  
16  
17 [(COD)Pt(OSi(O<sup>t</sup>Bu)<sub>3</sub>)]<sub>2</sub>Zn<sup>II</sup>/SiO<sub>2</sub> (**3\_Zn/SiO<sub>2</sub>**): A colourless solution of  
18 [Zn(OSi(O<sup>t</sup>Bu)<sub>3</sub>)<sub>2</sub>]<sub>2</sub> (0.234 g, 0.395 mmol) in benzene (10 ml) was added slowly to a suspension  
19 of SiO<sub>2-700</sub> (1.517 g, 0.455 mmol -OH) in benzene (10 ml) while stirring (100 rpm). The resulting  
20 suspension was stirred for 5 h at room temperature. The supernatant was removed, and the material  
21 washed with benzene (10 ml) three times to wash off unreacted complex. The material was then  
22 washed with pentane and subsequently dried under high vacuum (10<sup>-5</sup> mbar) for 3 h to remove  
23 residual solvent. The resulting white solid was then transferred to a tubular quartz reactor and  
24 treated under high vacuum (10<sup>-5</sup> mbar) at high temperature (r.t. to 300 °C (5 °C/min) for 1 h, 400  
25 °C (5 °C/min) for 1 h, 500 °C (5 °C/min) for 1 h, 600 °C (5 °C/min) for 8 h). Part of the resulting  
26 white solid (1.193 g, 0.358 mmol –OH assumed) was suspended in benzene (10 ml), and a  
27 colourless solution of **3** (0.258 g, 0.311 mmol) in benzene (10 ml) added to it slowly while stirring  
28  
29  
30  
31  
32  
33  
34  
35  
36  
37  
38  
39  
40  
41  
42  
43  
44  
45  
46  
47  
48  
49  
50  
51  
52  
53  
54  
55  
56  
57  
58  
59  
60

(100 rpm). The resulting suspension was stirred for 4 h at room temperature. The supernatant was removed, and the material washed with benzene (10 ml) three times to wash off unreacted complex. The material was then washed with pentane and subsequently dried under high vacuum ( $10^{-5}$  mbar) for 3 h to remove residual solvent. **3\_Zn/SiO<sub>2</sub>** was obtained as a white solid. Elemental Analysis: 2.77 wt.% Pt, 1.48 wt.% Zn.

**[(COD)Pt(OSi(OtBu)<sub>3</sub>)]\_Ga<sup>III</sup>/SiO<sub>2-700</sub> (3\_Ga/SiO<sub>2</sub>):** A colourless solution of [Ga(THF)(OSi(OtBu)<sub>3</sub>)<sub>3</sub>] (0.245 g, 0.263 mmol) in benzene (10 ml) was added slowly to a suspension of SiO<sub>2-700</sub> (1.009 g, 0.303 mmol -OH) in benzene (10 ml) while stirring (100 rpm). The resulting suspension was stirred for 12 h at room temperature. The supernatant was removed, and the material washed with benzene (10 ml) three times to wash off unreacted complex. The material was then washed with pentane and subsequently dried under high vacuum ( $10^{-5}$  mbar) for 5 h to remove residual solvent. The resulting white solid was then transferred to a tubular quartz reactor and treated under high vacuum ( $10^{-5}$  mbar) at high temperature (r.t. to 300 °C (5 °C/min) for 1 h, 400 °C (5 °C/min) for 1 h, 500 °C (5 °C/min) for 1 h, 600 °C (5 °C/min) for 8 h). Part of the resulting grey solid (0.480 g, 0.144 mmol -OH assumed) was suspended in benzene (10 ml), and a colourless solution of **3** (0.104 g, 0.125 mmol) in benzene (10 ml) added to it slowly while stirring (100 rpm). The resulting suspension was stirred for 12 h at room temperature. The supernatant was removed, and the material washed with benzene (10 ml) three times to wash off unreacted complex. The material was then washed with pentane and subsequently dried under high vacuum ( $10^{-5}$  mbar) for 3 h to remove residual solvent. **3\_Ga/SiO<sub>2</sub>** was obtained as a white solid.

**[(COD)PtMe]/SiO<sub>2-700</sub> (4/SiO<sub>2</sub>):** A colourless solution of **4** (0.087 g, 0.15 mmol) in benzene (10 mL) was added slowly to a suspension of SiO<sub>2-700</sub> (0.500 g, 0.15 mmol -OH) in benzene (10 mL) while stirring (100 rpm). The resulting suspension was stirred for 12 h at room

1  
2  
3 temperature. The supernatant was removed, and the material washed with benzene (10 mL) three  
4  
5 times to wash off unreacted complex. The material was then washed with pentane and dried under  
6  
7 high vacuum ( $10^{-5}$  mbar) for 4 h to remove residual solvent. **4/SiO<sub>2</sub>** was obtained as a white solid.  
8  
9 Elemental analysis: Pt, 4.96 wt. %.

10  
11  
12 **[(DMPE)PtMe]/SiO<sub>2-700</sub> (5/SiO<sub>2</sub>)**: A suspension of off-white/brown **5** (0.035 g, 0.093  
13  
14 mmol) in benzene (10 mL) was added slowly to a suspension of SiO<sub>2-700</sub> (0.311 g, 0.093 mmol  
15  
16 –OH) in benzene (10 mL) while stirring (100 rpm). The resulting suspension was stirred for 12 h  
17  
18 at room temperature with gradual disappearance of **5** in the suspension. The supernatant was  
19  
20 removed, and the material washed with benzene (10 mL) three times to wash off unreacted  
21  
22 complex. The material was then washed with pentane and dried under high vacuum ( $10^{-5}$  mbar)  
23  
24 for 2 h to remove residual solvent. **5/SiO<sub>2</sub>** was obtained as a white solid. Elemental analysis: 4.39  
25  
26 wt.% Pt; 1.35 wt.% P.  
27  
28  
29

30  
31 **Molecular DFT Calculations.** Atomic coordinates were optimized with DFT using  
32  
33 Gaussian09.<sup>101</sup> Geometry optimizations were performed using the B3LYP functional<sup>107</sup> in  
34  
35 combination with Pople's 6-31G(d) basis sets for H, C, Si atoms and 6-31+G(d) for negatively  
36  
37 charged atoms (P, O).<sup>108</sup> The Los Alamos LANL2TZ basis set was used for Pt atoms in conjunction  
38  
39 with the associated pseudopotential.<sup>109</sup> NMR calculations were performed using ADF 2016 with  
40  
41 the PBE0 functional and Slater-type basis sets of quadruple- $\zeta$  quality (QZ4P) for Pt and triple- $\zeta$   
42  
43 quality (TZP) for other atoms.<sup>102</sup> Relativistic effects were treated by the 2-component zeroth order  
44  
45 regular approximation (ZORA).<sup>95-96, 110</sup> The calculated <sup>195</sup>Pt chemical shifts were referenced to  
46  
47 (COD)PtCl<sub>2</sub>, with an experimental isotropic chemical shift of –3360 ppm, and a calculated  
48  
49 isotropic shielding of 5483 ppm. Calculated shielding tensors are plotted as 3D representations of  
50  
51  $\sum_{ij} r_i s_{ij} r_j$ , polar functions with scaling factors adjusted towards the best readability.<sup>111</sup>  
52  
53  
54  
55  
56  
57  
58  
59  
60



While the chemical shift ( $\delta$ ) is always reported with respect to a reference compound, DFT calculations output the magnetic shielding with respect to the bare nucleus ( $\sigma$ ); the equation below is used to convert calculated shielding values to chemical shift values, which are ordered so that  $\delta_{11} > \delta_{22} > \delta_{33}$ .

$$\begin{pmatrix} \delta_{11} & 0 & 0 \\ 0 & \delta_{22} & 0 \\ 0 & 0 & \delta_{33} \end{pmatrix} = \sigma_{\text{iso}}^{\text{ref}} \begin{pmatrix} 1 & 0 & 0 \\ 0 & 1 & 0 \\ 0 & 0 & 1 \end{pmatrix} - \begin{pmatrix} \sigma_{11} & 0 & 0 \\ 0 & \sigma_{22} & 0 \\ 0 & 0 & \sigma_{33} \end{pmatrix} \quad (1)$$

**Plane-wave DFT Calculations.** The hydrogen atom positions of Pt(acac)<sub>2</sub> in the previously reported crystal structure<sup>91</sup> were optimized using plane-wave density functional theory (DFT). The CASTEP<sup>112</sup> program was used with the PBE-GGA functional<sup>113</sup> and the TS dispersion correction scheme.<sup>114</sup> A  $k$ -point spacing of 0.07 Å<sup>-1</sup> was used for the Monkhorst-Pack grid.

**Solid-State NMR Experiments.** All experiments were performed at 9.4 T using a Bruker Avance III HD console. <sup>1</sup>H, <sup>31</sup>P and <sup>195</sup>Pt chemical shifts were indirectly referenced to tetramethylsilane using the <sup>1</sup>H shift of adamantane at 1.82 ppm. Analytical simulations were performed with the TopSpin solid lineshape analysis module (sola) or ssNake v1.1.<sup>115</sup>

*Fast MAS <sup>1</sup>H{<sup>195</sup>Pt} NMR Experiments.* A Bruker 1.3 mm HX probe and the MAS frequency was 50 kHz unless mentioned otherwise. Cisplatin and L-histidine·HCl·H<sub>2</sub>O were purchased and used as received from Alfa Aesar and Fluka, respectively; rotors of these samples were packed under ambient conditions. All other rotors were packed in an argon glovebox and rotors were spun with nitrogen gas. <sup>1</sup>H{<sup>195</sup>Pt} TONE D-HMQC-4 and PE RESPDOR experiments were performed using SR4<sub>1</sub><sup>2</sup> dipolar recoupling<sup>85</sup> that was applied at the 2<sup>nd</sup> order R<sup>3</sup> condition.<sup>116</sup> <sup>1</sup>H 90° and 180° pulse durations of 2.5 and 5 μs, respectively were used. The <sup>195</sup>Pt sideband-selective pulses were optimized by determining the rf fields that maximized D-HMQC signal

1  
2  
3 intensities using different pulse lengths (Table S1), with longer duration pulses providing more  
4  
5 selectivity (Figure S3-S4). The  $^1\text{H}\{^{71}\text{Ga}\}$  PE RESPDOR experiment used  $30\ \mu\text{s}$   $^{71}\text{Ga}$  saturation  
6  
7 pulses with a 330 kHz rf field. In  $^1\text{H}\{^{195}\text{Pt}\}$  TONE D-HMQC-4 experiments, SHAPs used tanh/tan  
8  
9 shapes with a  $20\ \mu\text{s}$  duration, *ca.* 275 kHz rf field and 5 MHz sweep width. Lee-Goldburg spinlock  
10  
11 pulses of *ca.* 1 ms total duration were applied at a rf field of 150 kHz at the appropriate transmitter  
12  
13 offset frequency.<sup>86, 117</sup> For sideband-selective  $^1\text{H}\{^{195}\text{Pt}\}$  TONE D-HMQC-4 experiments the  $^{195}\text{Pt}$   
14  
15 offset for the SHAP inversion pulses was held constant, approximately in the center of NMR  
16  
17 powder pattern, while the offset of the sideband-selective pulses was varied. For both TONE D-  
18  
19 HMQC-4 and PE RESPDOR sideband-selective experiments the probe was not retuned for each  
20  
21 offset. Retuning the probe was found to have a minimal effect on sideband intensities (Figure S5).  
22  
23  
24  
25

26 Total  $SR4_1^2$  dipolar recoupling durations of 1.92 ms (**1**, TONE D-HMQC-4), 2.88 ms (**1**,  
27  
28 PE RESPDOR), 3.2 ms (**2**, TONE D-HMQC-4 and PE RESPDOR), 1.76 ms (**3/SiO<sub>2</sub>**, TONE D-  
29  
30 HMQC-4), 2.08 ms (**3/SiO<sub>2</sub>**, PE RESPDOR), 2.56 ms (**4/SiO<sub>2</sub>**, TONE D-HMQC-4) and 2.4 ms  
31  
32 (**3\_Zn/SiO<sub>2</sub>** and **3\_Ga/SiO<sub>2</sub>**, PE RESPDOR) were used in the various sideband-selective  
33  
34 experiments. For the molecular compounds and silica-supported compounds  $60\ \mu\text{s}$ , 9 kHz rf field  
35  
36 and  $40\ \mu\text{s}$ , 16 kHz rf field sideband-selective saturation pulses were employed, respectively. For  
37  
38 **4/SiO<sub>2</sub>**  $40\ \mu\text{s}$  sideband-selective pulses with a 12 kHz rf field were used. In case of **1**, although the  
39  
40 maximum dephasing observed with PE RESPDOR was only *ca.* 9% with a total recoupling  
41  
42 duration of 2.88 ms, the tolerance to MAS instability is higher at shorter recoupling durations (only  
43  
44 0.7% variation of the RESPDOR  $S_0$  signal intensity was observed, which is the primary source of  
45  
46 error in the measurements, Figure S7A). A longer recoupling duration provides more dephasing  
47  
48 (Figure S7D) but results in a ‘noisier’  $^{195}\text{Pt}$  sideband manifold (Figure S11). Therefore, recoupling  
49  
50  
51  
52  
53  
54  
55  
56  
57  
58  
59  
60

1  
2  
3 durations shorter than that providing maximal dephasing may be preferred for the variable offset  
4  
5 PE RESPDOR experiments.  
6

7  
8 The experimental  $^{195}\text{Pt}$  sideband-selective patterns are best reproduced by numerical  
9  
10 simulations, as performed here using SIMPSON (*vide infra*). Alternatively, an approximate  
11  
12 estimate of the CSA values can be obtained using Herzfeld-Berger analysis (HBA).<sup>118-119</sup> For  
13  
14 example, with cisplatin, the isotropic shift was fixed to  $-1834$  ppm while  $\Omega$  and  $\kappa$  were fitted using  
15  
16 the HBA program. The estimated CSA parameters for cisplatin were  $\Omega = 9776$  ppm and  $\kappa = -0.65$   
17  
18 with TONE D-HMQC-4, and  $\Omega = 9584$  ppm and  $\kappa = -0.64$  with PE RESPDOR (Figure S32). The  
19  
20 HBA program used for fitting assumes ideal sideband intensities during fitting; however, the  
21  
22 intensities of the  $^{195}\text{Pt}$  pattern from the sideband-selective experiments deviate from the ideal  
23  
24 pattern and can only be reproduced using numerical simulations. Therefore, HBA should be  
25  
26 performed only to estimate the  $^{195}\text{Pt}$  CSA.  
27  
28  
29  
30

31  $^{31}\text{P}\{^{195}\text{Pt}\}$  NMR Experiments. All  $^1\text{H}-^{31}\text{P}\{^{195}\text{Pt}\}$  experiments were performed using a  
32  
33 Bruker 2.5 mm HXY probe. The pulse sequences used for the acquisition of  $^1\text{H}-^{31}\text{P}\{^{195}\text{Pt}\}$  CP  $J$ -  
34  
35 HMQC and sideband-selective  $J$ -resolved spectra are shown in Figure S27. Pulse durations of 2.5  
36  
37  $\mu\text{s}$  ( $\pi/2$ ,  $^1\text{H}$ ), 4.75  $\mu\text{s}$  ( $\pi$ ,  $^{31}\text{P}$ ) and 2-2.5  $\mu\text{s}$  ( $\pi/2$ ,  $^{195}\text{Pt}$ ) were used. The constant-time 2D  $^1\text{H}$ -  
38  
39  $^{31}\text{P}\{^{195}\text{Pt}\}$  CP  $J$ -HMQC spectrum of **5** was acquired with 12.5 kHz MAS, 8 scans, 1.5 s recycle  
40  
41 delay ( $1.3 \times T_1$ ), indirect spectral width of 500 kHz, 822 complex  $t_1$ -increments and a total  $J$ -  
42  
43 evolution time ( $2 \times m \times \tau_r$ ) of 1.28 ms (Figure 6C). The  $^1\text{H} \rightarrow ^{31}\text{P}$  CP duration was set to 2.5 ms and  
44  
45 optimal  $^1\text{H}$  and  $^{31}\text{P}$  spinlock rf powers of 75 kHz and 83 kHz, respectively, were used; the  $^1\text{H}$  rf  
46  
47 power was ramped from 85-100%. For all experiments with **5/SiO<sub>2</sub>**, a  $^1\text{H} \rightarrow ^{31}\text{P}$  CP duration of 5  
48  
49 ms and optimal  $^1\text{H}$  and  $^{31}\text{P}$  spinlock rf powers of 105 kHz and 83 kHz, respectively, were used;  
50  
51 the  $^1\text{H}$  rf power was ramped from 90-100%. The sideband-selective  $^1\text{H}-^{31}\text{P}\{^{195}\text{Pt}\}$  CP  $J$ -resolved  
52  
53  
54  
55  
56  
57  
58  
59  
60

1  
2  
3 spectra of **5/SiO<sub>2</sub>** was acquired with 25 kHz MAS, 1800 scans and 1.5 s recycle delay per point;  
4  
5 the total *J*-evolution time ( $2 \times m \times \tau_r$ ) was set to 560  $\mu$ s, and a 40  $\mu$ s <sup>195</sup>Pt saturation pulse at 22 kHz  
6  
7 rf was applied. The offset was incremented in steps of the MAS frequency and 21 sub-spectra were  
8  
9 obtained. The total duration of each echo in the CPMG train was set to 800  $\mu$ s and 55 spin echoes  
10  
11 were acquired. 100 kHz SPINAL-64 decoupling was applied during *J*-evolution periods and signal  
12  
13 acquisition.<sup>120</sup>  
14  
15

16  
17 *SIMPSON simulations.* All <sup>1</sup>H{<sup>195</sup>Pt} SIMPSON simulations were performed with a 50  
18  
19 kHz MAS frequency and a <sup>1</sup>H Larmor frequency of 400.498 MHz. The <sup>1</sup>H-<sup>195</sup>Pt dipolar coupling  
20  
21 was set to -3500 Hz and an optimal recoupling duration of 2.88 ms was used. For the simulations  
22  
23 shown in Figure 2, the rep168 crystal file and 24 gamma angles were used for powder averaging.  
24  
25 For all other simulations in the main text, the rep320 crystal file and 13 gamma angles were used.  
26  
27 60  $\mu$ s selective excitation pulses with an optimized 9 kHz rf field were used in the simulations for  
28  
29 all molecular compounds, whereas shorter 40  $\mu$ s duration pulses at 16 kHz rf were used for the  
30  
31 surface compounds. The optimal rf fields for the sideband-selective excitation pulses in D-HMQC  
32  
33 agree well between simulations and experiments (Table S1). In all cases, the offset frequency of a  
34  
35 sideband was determined by first varying the offset in small steps of 1-2 kHz, followed by stepping  
36  
37 the transmitter offset in steps equal to the MAS frequency. Note that the TONE D-HMQC-2  
38  
39 sequence was used for SIMPSON simulations throughout this work, while TONE D-HMQC-4 was  
40  
41 used for experiments. TONE D-HMQC-2 was used for simulations because TONE D-HMQC-4  
42  
43 relies on experimental rf inhomogeneity, which is absent in the simulations, to dephase  
44  
45 uncorrelated signals.<sup>86</sup> The sideband-selective <sup>31</sup>P{<sup>195</sup>Pt} *J*-resolved experiments with **5/SiO<sub>2</sub>** were  
46  
47 simulated using a <sup>31</sup>P-<sup>195</sup>Pt *J*-coupling of 1825 Hz, a *J*-evolution time of 560  $\mu$ s, and a 25 kHz  
48  
49 MAS frequency as in the experiments.  
50  
51  
52  
53  
54  
55  
56  
57  
58  
59  
60

1  
2  
3 Plots showing the root mean square deviation (RMSD) between experimental and  
4 simulated patterns are provided in the SI for all samples. Briefly, the sideband NMR spectra were  
5 fit with the following procedure: (i) visual inspection of the sideband manifold provides a  
6 preliminary estimate of the principal components of the CSA tensor, (ii) the skew of the CS tensor  
7 was fixed while the span was varied and (iii) finally, the span with the lowest RMSD was fixed  
8 and the skew was varied to determine the best fit.  
9  
10  
11  
12  
13  
14  
15  
16

### 17 **Acknowledgements**

18 This work was primarily supported by a grant from the National Science Foundation CBET-  
19 1916809 to AJR. The development of sideband-selective NMR methods was supported by the U.S.  
20 Department of Energy (DOE), Office of Science, Basic Energy Sciences, Materials Science and  
21 Engineering Division. The Ames Laboratory is operated for the U.S. DOE by Iowa State  
22 University under contract # DE-AC02-07CH11358. AJR acknowledges additional support from  
23 the Alfred P. Sloan Foundation through a Sloan research fellowship. The research carried out at  
24 ETH Zürich was partially funded by the Swiss National Science Foundation (Grant number  
25 200021\_169134 and 200020B\_192050). This work is part of a project that has received funding  
26 from the European Union's Horizon 2020 research and innovation programme under Grant  
27 Agreement No 101008500 ("PANACEA"). This work is also supported by the Common Research  
28 Laboratory CARMEN (ENS de Lyon, CNRS, IFPEN, Claude Bernard Lyon 1 University,  
29 Sorbonne University, and University of Strasbourg). We are grateful to Ribal Jabbour for his help  
30 with the setup of static  $^{195}\text{Pt}$  solid-state NMR experiments. Dr. Christopher Gordon is also  
31 gratefully acknowledged for discussions on NMR computations.  
32  
33  
34  
35  
36

### 37 **Supporting Information**

38 Additional experimental and simulated NMR spectra, and experimental details can be found in the  
39 supporting information. Pulse sequences, SIMPSON simulation input files, and raw NMR data for  
40 main text Figures are available for download at <https://doi.org/10.5281/zenodo.6639016>.  
41  
42  
43  
44  
45  
46  
47  
48  
49  
50  
51  
52  
53  
54  
55  
56  
57  
58  
59  
60

## References

1. Bowker, M. *The Basis and Applications of Heterogeneous Catalysis*. Oxford University Press: Oxford, 1998.
2. Fechete, I.; Wang, Y.; Vedrine, J. C. The Past, Present and Future of Heterogeneous Catalysis. *Catal. Today* **2012**, *189* (1), 2-27.
3. Friend, C. M.; Xu, B. J. Heterogeneous Catalysis: A Central Science for a Sustainable Future. *Acc. Chem. Res.* **2017**, *50* (3), 517-521.
4. Coperet, C. Fuels and Energy Carriers from Single-Site Catalysts Prepared via Surface Organometallic Chemistry. *Nat. Energy* **2019**, *4* (12), 1018-1024.
5. Tennakoon, A.; Wu, X.; Paterson, A. L.; Patnaik, S.; Pei, Y. C.; LaPointe, A. M.; Ammal, S. C.; Hackler, R. A.; Heyden, A.; Slowing, I. I.; Coates, G. W.; Delferro, M.; Peters, B.; Huang, W. Y.; Sadow, A. D.; Perras, F. A. Catalytic Upcycling of High-Density Polyethylene via a Processive Mechanism. *Nat. Catal.* **2020**, *3* (11), 893-901.
6. Thomas, J. M.; Raja, R.; Lewis, D. W. Single-Site Heterogeneous Catalysts. *Angew. Chem. Int. Ed.* **2005**, *44* (40), 6456-6482.
7. Korzyński, M. D.; Copéret, C. Single Sites in Heterogeneous Catalysts: Separating Myth from Reality. *Trends Chem.* **2021**, *3* (10), 850-862.
8. Wang, A. Q.; Li, J.; Zhang, T. Heterogeneous Single-Atom Catalysis. *Nat. Rev. Chem.* **2018**, *2* (6), 65-81.
9. Wegener, S. L.; Marks, T. J.; Stair, P. C. Design Strategies for the Molecular Level Synthesis of Supported Catalysts. *Acc. Chem. Res.* **2012**, *45* (2), 206-214.
10. Coperet, C.; Comas-Vives, A.; Conley, M. P.; Estes, D. P.; Fedorov, A.; Mougél, V.; Nagae, H.; Nunez-Zarur, F.; Zhizhko, P. A. Surface Organometallic and Coordination Chemistry toward Single-Site Heterogeneous Catalysts: Strategies, Methods, Structures, and Activities. *Chem. Rev.* **2016**, *116* (2), 323-421.
11. Pelletier, J. D. A.; Basset, J. M. Catalysis by Design: Well-Defined Single-Site Heterogeneous Catalysts. *Acc. Chem. Res.* **2016**, *49* (4), 664-677.
12. Laurent, P.; Veyre, L.; Thieuleux, C.; Donet, S.; Coperet, C. From Well-Defined Pt(II) Surface Species to the Controlled Growth of Silica Supported Pt Nanoparticles. *Dalton Trans.* **2013**, *42* (1), 238-248.
13. Searles, K.; Chan, K. W.; Burak, J. A. M.; Zemlyanov, D.; Safonova, O.; Coperet, C. Highly Productive Propane Dehydrogenation Catalyst Using Silica-Supported Ga-Pt Nanoparticles Generated from Single-Sites. *J. Am. Chem. Soc.* **2018**, *140* (37), 11674-11679.
14. Coperet, C. Single-Sites and Nanoparticles at Tailored Interfaces Prepared via Surface Organometallic Chemistry from Thermolytic Molecular Precursors. *Acc. Chem. Res.* **2019**, *52* (6), 1697-1708.
15. Rochlitz, L.; Searles, K.; Alfke, J.; Zemlyanov, D.; Safonova, O. V.; Coperet, C. Silica-Supported, Narrowly Distributed, Subnanometric Pt-Zn Particles from Single Sites with High Propane Dehydrogenation Performance. *Chem. Sci.* **2020**, *11* (6), 1549-1555.
16. Payard, P. A.; Rochlitz, L.; Searles, K.; Foppa, L.; Leuthold, B.; Safonova, O. V.; Comas-Vives, A.; Copéret, C. Dynamics and Site Isolation: Keys to High Propane Dehydrogenation Performance of Silica-Supported PtGa Nanoparticles. *JACS Au* **2021**, *1* (9), 1445-1458.
17. Zhang, W. P.; Xu, S. T.; Han, X. W.; Bao, X. H. In Situ Solid-State NMR for Heterogeneous Catalysis: A Joint Experimental and Theoretical Approach. *Chem. Soc. Rev.* **2012**, *41* (1), 192-210.
18. D'Elia, V.; Dong, H. L.; Rossini, A. J.; Widdifield, C. M.; Vummaleti, S. V. C.; Minenkov, Y.; Poater, A.; Abou-Hamad, E.; Pelletier, J. D. A.; Cavallo, L.; Emsley, L.; Basset, J. M. Cooperative Effect of Monopodal Silica-Supported Niobium Complex Pairs Enhancing Catalytic Cyclic Carbonate Production. *J. Am. Chem. Soc.* **2015**, *137* (24), 7728-7739.
19. Kobayashi, T.; Perras, F. A.; Slowing, I. I.; Sadow, A. D.; Pruski, M. Dynamic Nuclear Polarization Solid-State NMR in Heterogeneous Catalysis Research. *ACS Catal.* **2015**, *5* (12), 7055-7062.

- 1  
2  
3 20. Coperet, C.; Liao, W. C.; Gordon, C. P.; Ong, T. C. Active Sites in Supported Single-Site  
4 Catalysts: An NMR Perspective. *J. Am. Chem. Soc.* **2017**, *139* (31), 10588-10596.
- 5 21. Vancompernelle, T.; Trivelli, X.; Delevoeye, L.; Pourpoint, F.; Gauvin, R. M. On the use of Solid-  
6 State  $^{45}\text{Sc}$  NMR for Structural Investigations of Molecular and Silica-Supported Scandium Amide  
7 Catalysts. *Dalton Trans.* **2017**, *46* (39), 13176-13179.
- 8 22. Grekov, D.; Vancompernelle, T.; Taoufik, M.; Delevoeye, L.; Gauvin, R. M. Solid-State NMR of  
9 Quadrupolar Nuclei for Investigations into Supported Organometallic Catalysts: Scope and Frontiers.  
10 *Chem. Soc. Rev.* **2018**, *47* (8), 2572-2590.
- 11 23. Culver, D. B.; Venkatesh, A.; Huynh, H.; Rossini, A. J.; Conley, M. P.  $\text{Al}(\text{OR}^{\text{F}})_3$  ( $\text{R}^{\text{F}} = \text{C}(\text{CF}_3)_3$ )  
12 Activated Silica: A Well-Defined Weakly Coordinating Surface Anion. *Chem. Sci.* **2020**, *11* (6), 1510-  
13 1517.
- 14 24. Berruyer, P.; Lelli, M.; Conley, M. P.; Silverio, D. L.; Widdifield, C. M.; Siddiqi, G.; Gajan, D.;  
15 Lesage, A.; Coperet, C.; Emsley, L. Three-Dimensional Structure Determination of Surface Sites. *J. Am.*  
16 *Chem. Soc.* **2017**, *139* (2), 849-855.
- 17 25. Perras, F. A.; Paterson, A. L.; Syed, Z. H.; Kropf, A. J.; Kaphan, D. M.; Delferro, M.; Pruski, M.  
18 Revealing the Configuration and Conformation of Surface Organometallic Catalysts with DNP-Enhanced  
19 NMR. *J. Phys. Chem. C* **2021**, *125* (24), 13433-13442.
- 20 26. Zilm, K. W.; Conlin, R. T.; Grant, D. M.; Michl, J. Low-Temperature Natural-Abundance  
21 Carbon-13 NMR Spectroscopy of Matrix-Isolated Species - Anisotropy of Shielding Tensor in Ethylene.  
22 *J. Am. Chem. Soc.* **1978**, *100* (25), 8038-8039.
- 23 27. Widdifield, C. M.; Schurko, R. W. Understanding Chemical Shielding Tensors Using Group  
24 Theory, MO Analysis, and Modern Density-Functional Theory. *Concepts Magn. Reson. Part A* **2009**, *34a*  
25 (2), 91-123.
- 26 28. Facelli, J. C. Chemical Shift Tensors: Theory and Application to Molecular Structural Problems.  
27 *Prog. Nucl. Magn. Reson. Spectrosc.* **2011**, *58* (3-4), 176-201.
- 28 29. Gordon, C. P.; Raynaud, C.; Andersen, R. A.; Coperet, C.; Eisenstein, O. Carbon-13 NMR  
29 Chemical Shift: A Descriptor for Electronic Structure and Reactivity of Organometallic Compounds. *Acc.*  
30 *Chem. Res.* **2019**, *52* (8), 2278-2289.
- 31 30. Halbert, S.; Coperet, C.; Raynaud, C.; Eisenstein, O. Elucidating the Link between NMR  
32 Chemical Shifts and Electronic Structure in  $d(0)$  Olefin Metathesis Catalysts. *J. Am. Chem. Soc.* **2016**,  
33 *138* (7), 2261-2272.
- 34 31. Lummiss, J. A. M.; Perras, F. A.; McDonald, R.; Bryce, D. L.; Fogg, D. E. Sterically Driven  
35 Olefin Metathesis: The Impact of Alkylidene Substitution on Catalyst Activity. *Organometallics* **2016**, *35*  
36 (5), 691-698.
- 37 32. Yamamoto, K.; Gordon, C. P.; Liao, W. C.; Coperet, C.; Raynaud, C.; Eisenstein, O. Orbital  
38 Analysis of Carbon-13 Chemical Shift Tensors Reveals Patterns to Distinguish Fischer and Schrock  
39 Carbenes. *Angew. Chem. Int. Ed.* **2017**, *56* (34), 10127-10131.
- 40 33. Culver, D. B.; Huynh, W.; Tafazolian, H.; Ong, T. C.; Conley, M. P. The beta-Agostic Structure  
41 in  $(\text{C}_5\text{Me}_5)_2\text{Sc}(\text{CH}_2\text{CH}_3)$ : Solid-State NMR Studies of  $(\text{C}_5\text{Me}_5)_2\text{Sc-R}$  ( $\text{R} = \text{Me}, \text{Ph}, \text{Et}$ ). *Angew. Chem. Int.*  
42 *Ed.* **2018**, *57* (30), 9520-9523.
- 43 34. Hillenbrand, J.; Leutzsch, M.; Gordon, C. P.; Coperet, C.; Furstner, A.  $^{183}\text{W}$  NMR Spectroscopy  
44 Guides the Search for Tungsten Alkylidyne Catalysts for Alkyne Metathesis. *Angew. Chem. Int. Ed.*  
45 **2020**, *59* (48), 21758-21768.
- 46 35. Pietrasiak, E.; Gordon, C. P.; Coperet, C.; Togni, A. Understanding  $^{125}\text{Te}$  NMR chemical shifts in  
47 Disymmetric Organo-Telluride Compounds from Natural Chemical Shift Analysis. *Phys. Chem. Chem.*  
48 *Phys.* **2020**, *22* (4), 2319-2326.
- 49 36. Arduengo, A. J.; Dixon, D. A.; Kumashiro, K. K.; Lee, C.; Power, W. P.; Zilm, K. W. Chemical  
50 Shielding Tensor of a Carbene. *J. Am. Chem. Soc.* **1994**, *116* (14), 6361-6367.
- 51 37. Vummaleti, S. V. C.; Nelson, D. J.; Poater, A.; Gomez-Suarez, A.; Cordes, D. B.; Slawin, A. M.  
52 Z.; Nolan, S. P.; Cavallo, L. What can NMR Spectroscopy of Selenoureas and Phosphinidenes Teach us  
53 About the Pi-Accepting Abilities of N-heterocyclic Carbenes? *Chem. Sci.* **2015**, *6* (3), 1895-1904.
- 54  
55  
56  
57  
58  
59  
60

- 1  
2  
3 38. Engl, P. S.; Santiago, C. B.; Gordon, C. P.; Liao, W. C.; Fedorov, A.; Coperet, C.; Sigman, M. S.;  
4 Togni, A. Exploiting and Understanding the Selectivity of Ru-N-Heterocyclic Carbene Metathesis  
5 Catalysts for the Ethenolysis of Cyclic Olefins to alpha,omega-Dienes. *J. Am. Chem. Soc.* **2017**, *139* (37),  
6 13117-13125.
- 7 39. Taoufik, M.; Szeto, K. C.; Merle, N.; Del Rosal, I.; Maron, L.; Trebosc, J.; Tricot, G.; Gauvin, R.  
8 M.; Delevoye, L. Heteronuclear NMR Spectroscopy as a Surface-Selective Technique: A Unique Look at  
9 the Hydroxyl Groups of gamma-Alumina. *Chem. Eur. J.* **2014**, *20* (14), 4038-4046.
- 10 40. Mance, D.; Comas-Vives, A.; Coperet, C. Proton-Detected Multidimensional Solid-State NMR  
11 Enables Precise Characterization of Vanadium Surface Species at Natural Abundance. *J. Phys. Chem.*  
12 *Lett.* **2019**, *10* (24), 7898-7904.
- 13 41. Love, A. M.; Cendejas, M. C.; Hanrahan, M. P.; Carnahan, S. L.; Uchupalanun, P.; Rossini, A. J.;  
14 Hermans, I. Understanding the Synthesis of Supported Vanadium Oxide Catalysts Using Chemical  
15 Grafting. *Chem. Eur. J.* **2020**, *26* (5), 1052-1063.
- 16 42. Corma, A.; Nemeth, L. T.; Renz, M.; Valencia, S. Sn-zeolite Beta as a Heterogeneous  
17 Chemoselective Catalyst for Baeyer-Villiger Oxidations. *Nature* **2001**, *412* (6845), 423-5.
- 18 43. Merle, N.; Trebosc, J.; Baudouin, A.; Rosal, I. D.; Maron, L.; Szeto, K.; Genelot, M.; Mortreux,  
19 A.; Taoufik, M.; Delevoye, L.; Gauvin, R. M. <sup>17</sup>O NMR gives Unprecedented Insights into the Structure  
20 of Supported Catalysts and their Interaction with the Silica Carrier. *J. Am. Chem. Soc.* **2012**, *134* (22),  
21 9263-75.
- 22 44. Gunther, W. R.; Michaelis, V. K.; Caporini, M. A.; Griffin, R. G.; Roman-Leshkov, Y. Dynamic  
23 Nuclear Polarization NMR Enables the Analysis of Sn-Beta Zeolite Prepared with Natural Abundance  
24 <sup>119</sup>Sn Precursors. *J. Am. Chem. Soc.* **2014**, *136* (17), 6219-22.
- 25 45. Delley, M. F.; Lapadula, G.; Nunez-Zarur, F.; Comas-Vives, A.; Kalendra, V.; Jeschke, G.;  
26 Baabe, D.; Walter, M. D.; Rossini, A. J.; Lesage, A.; Emsley, L.; Maury, O.; Coperet, C. Local Structures  
27 and Heterogeneity of Silica-Supported M(III) Sites Evidenced by EPR, IR, NMR, and Luminescence  
28 Spectroscopies. *J. Am. Chem. Soc.* **2017**, *139* (26), 8855-8867.
- 29 46. Camacho-Bunquin, J.; Ferrandon, M.; Sohn, H.; Yang, D. L.; Liu, C.; Ignacio-de Leon, P. A.;  
30 Perras, F. A.; Pruski, M.; Stair, P. C.; Delferro, M. Chemoselective Hydrogenation with Supported  
31 Organoplatinum(IV) Catalyst on Zn(II)-Modified Silica. *J. Am. Chem. Soc.* **2018**, *140* (11), 3940-3951.
- 32 47. Perras, F. A.; Boteju, K. C.; Slowing, II; Sadow, A. D.; Pruski, M. Direct <sup>17</sup>O Dynamic Nuclear  
33 Polarization of Single-Site Heterogeneous Catalysts. *Chem. Commun.* **2018**, *54* (28), 3472-3475.
- 34 48. Nagashima, H.; Trebosc, J.; Kon, Y.; Sato, K.; Lafon, O.; Amoureux, J. P. Observation of Low-  
35 gamma Quadrupolar Nuclei by Surface-Enhanced NMR Spectroscopy. *J. Am. Chem. Soc.* **2020**, *142* (24),  
36 10659-10672.
- 37 49. Ishizaka, Y.; Arai, N.; Matsumoto, K.; Nagashima, H.; Takeuchi, K.; Fukaya, N.; Yasuda, H.;  
38 Sato, K.; Choi, J. C. Bidentate Disilicate Framework for Bis-Grafted Surface Species. *Chem. Eur. J.*  
39 **2021**, *27* (47), 12069-12077.
- 40 50. Fu, Q.; Saltsburg, H.; Flytzani-Stephanopoulos, M. Active Nonmetallic Au and Pt Species on  
41 Ceria-based Water-Gas Shift Catalysts. *Science* **2003**, *301* (5635), 935-938.
- 42 51. Vajda, S.; Pellin, M. J.; Greeley, J. P.; Marshall, C. L.; Curtiss, L. A.; Ballentine, G. A.; Elam, J.  
43 W.; Catillon-Mucherie, S.; Redfern, P. C.; Mehmood, F.; Zapol, P. Subnanometre Platinum Clusters as  
44 Highly Active and Selective Catalysts for the Oxidative Dehydrogenation of Propane. *Nat. Mater.* **2009**, *8*  
45 (3), 213-216.
- 46 52. Qiao, B. T.; Wang, A. Q.; Yang, X. F.; Allard, L. F.; Jiang, Z.; Cui, Y. T.; Liu, J. Y.; Li, J.;  
47 Zhang, T. Single-atom catalysis of CO oxidation using Pt-1/FeOx. *Nat. Chem.* **2011**, *3* (8), 634-641.
- 48 53. MacGregor, A. W.; O'Dell, L. A.; Schurko, R. W. New Methods for the Acquisition of Ultra-  
49 Wideline Solid-State NMR Spectra of Spin-1/2 Nuclides. *J. Magn. Reson.* **2011**, *208* (1), 103-113.
- 50 54. Schurko, R. W. Ultra-Wideline Solid-State NMR Spectroscopy. *Acc. Chem. Res.* **2013**, *46* (9),  
51 1985-1995.  
52  
53  
54  
55  
56  
57  
58  
59  
60



- 1  
2  
3 55. Lucier, B. E. G.; Johnston, K. E.; Xu, W. Q.; Hanson, J. C.; Senanayake, S. D.; Yao, S. Y.;  
4 Bourassa, M. W.; Srebro, M.; Autschbach, J.; Schurko, R. W. Unravelling the Structure of Magnus' Pink  
5 Salt. *J. Am. Chem. Soc.* **2014**, *136* (4), 1333-1351.
- 6 56. Austin, E. J. W.; Barrie, P. J.; Clark, R. J. H. Solid-State  $^{195}\text{Pt}$  NMR-Studies of the Complexes  
7  $\text{Pt}(\text{En})\text{Cl}_x$  (En = 1,2-Diaminoethane  $x = 2,3$  or 4). *J. Chem. Soc., Chem. Commun.* **1993**, (18), 1404-1405.
- 8 57. Sparks, S. W.; Ellis, P. D.  $^{195}\text{Pt}$  Shielding Tensors in Potassium Hexachloroplatinate(IV) and  
9 Potassium Tetrachloroplatinate(II). *J. Am. Chem. Soc.* **1986**, *108* (12), 3215-3218.
- 10 58. Sterzel, M.; Autschbach, J. Toward an Accurate Determination of  $^{195}\text{Pt}$  Chemical Shifts by  
11 Density Functional Computations: The Importance of Unspecific Solvent Effects and the Dependence of  
12 Pt Magnetic Shielding Constants on Structural Parameters. *Inorg. Chem.* **2006**, *45* (8), 3316-3324.
- 13 59. Autschbach, J.; Zheng, S. H. Analyzing Pt Chemical Shifts Calculated from Relativistic Density  
14 Functional Theory Using Localized Orbitals: The Role of Pt 5d Lone Pairs. *Magn. Reson. Chem.* **2008**,  
15 *46*, S45-S55.
- 16 60. Lucier, B. E. G.; Reidel, A. R.; Schurko, R. W. Multinuclear Solid-State NMR of Square-Planar  
17 Platinum Complexes - Cisplatin and Related Systems. *Can. J. Chem.* **2011**, *89* (7), 919-937.
- 18 61. Siegel, R.; Nakashima, T. T.; Wasylishen, R. E. Application of Multiple-Pulse Experiments to  
19 Characterize Broad NMR Chemical-Shift Powder Patterns from Spin-1/2 Nuclei in the Solid State. *J.*  
20 *Phys. Chem. B* **2004**, *108* (7), 2218-2226.
- 21 62. Harris, K. J.; Lupulescu, A.; Lucier, B. E. G.; Frydman, L.; Schurko, R. W. Broadband Adiabatic  
22 Inversion Pulses for Cross Polarization in Wideline Solid-State NMR Spectroscopy. *J. Magn. Reson.*  
23 **2012**, *224*, 38-47.
- 24 63. Altenhof, A. R.; Jaroszewicz, M. J.; Lindquist, A. W.; Foster, L. D. D.; Veinberg, S. L.; Schurko,  
25 R. W. Practical Aspects of Recording Ultra-Wideline NMR Patterns under Magic-Angle Spinning  
26 Conditions. *J. Phys. Chem. C* **2020**, *124* (27), 14730-14744.
- 27 64. Kobayashi, T.; Perras, F. A.; Goh, T. W.; Metz, T. L.; Huang, W. Y.; Pruski, M. DNP-Enhanced  
28 Ultrawideline Solid-State NMR Spectroscopy: Studies of Platinum in Metal-Organic Frameworks. *J.*  
29 *Phys. Chem. Lett.* **2016**, *7* (13), 2322-2327.
- 30 65. Kobayashi, T.; Perras, F. A.; Murphy, A.; Yao, Y.; Catalano, J.; Centeno, S. A.; Dybowski, C.;  
31 Zumbulyadis, N.; Pruski, M. DNP-Enhanced Ultrawideline Pb-207 Solid-State NMR Spectroscopy: an  
32 Application to Cultural Heritage Science. *Dalton Trans.* **2017**, *46* (11), 3535-3540.
- 33 66. Venkatesh, A.; Lund, A.; Rochlitz, L.; Jabbour, R.; Gordon, C. P.; Menzildjian, G.; Viger-Gravel,  
34 J.; Berruyer, P.; Gajan, D.; Copéret, C.; Lesage, A.; Rossini, A. J. The Structure of Molecular and Surface  
35 Platinum Sites Determined by DNP-SENS and Fast MAS  $^{195}\text{Pt}$  Solid-State NMR Spectroscopy. *J. Am.*  
36 *Chem. Soc.* **2020**, *142* (44), 18936-18945.
- 37 67. Ishii, Y.; Yesinowski, J. P.; Tycko, R. Sensitivity Enhancement in Solid-State  $^{13}\text{C}$  NMR of  
38 Synthetic Polymers and Biopolymers by  $^1\text{H}$  NMR Detection with High-Speed Magic Angle Spinning. *J.*  
39 *Am. Chem. Soc.* **2001**, *123* (12), 2921-2922.
- 40 68. Reif, B.; Griffin, R. G.  $^1\text{H}$  Detected  $^1\text{H}$ - $^{15}\text{N}$  Correlation Spectroscopy in Rotating Solids. *J. Magn.*  
41 *Reson.* **2003**, *160* (1), 78-83.
- 42 69. Poppler, A. C.; Demers, J. P.; Malon, M.; Singh, A. P.; Roesky, H. W.; Nishiyama, Y.; Lange, A.  
43 Ultrafast Magic-Angle Spinning: Benefits for the Acquisition of Ultrawide-Line NMR Spectra of Heavy  
44 Spin-1/2 Nuclei. *ChemPhysChem* **2016**, *17* (6), 812-816.
- 45 70. Kobayashi, T.; Nishiyama, Y.; Pruski, M. Heteronuclear Correlation Solid-state NMR  
46 Spectroscopy with Indirect Detection under Fast Magic-Angle Spinning. In *Modern Methods in Solid-*  
47 *state NMR: A Practitioner's Guide*, Hodgkinson, P., Ed. The Royal Society of Chemistry: **2018**; pp 1-38.
- 48 71. Rossini, A. J.; Hanrahan, M. P.; Thuo, M. Rapid Acquisition of Wideline MAS Solid-State NMR  
49 Spectra with Fast MAS, Proton Detection, and Dipolar HMQC Pulse Sequences. *Phys. Chem. Chem.*  
50 *Phys.* **2016**, *18* (36), 25284-25295.
- 51 72. Perras, F. A.; Venkatesh, A.; Hanrahan, M. P.; Goh, T. W.; Huang, W.; Rossini, A. J.; Pruski, M.  
52 Indirect Detection of Infinite-Speed MAS Solid-State NMR Spectra. *J. Magn. Reson.* **2017**, *276*, 95-102.
- 53  
54  
55  
56  
57  
58  
59  
60

- 1  
2  
3 73. Li, Y. X.; Trebosc, J.; Hu, B. W.; Shen, M.; Amoureux, J. P.; Lafon, O. Indirect detection of  
4 Broad Spectra in Solid-State NMR Using Interleaved DANTE Trains. *J. Magn. Reson.* **2018**, *294*, 101-  
5 114.
- 6 74. Venkatesh, A.; Perras, F. A.; Rossini, A. J. Proton-Detected Solid-State NMR Spectroscopy of  
7 Spin-1/2 Nuclei with Large Chemical Shift Anisotropy. *J. Magn. Reson.* **2021**, *327*, 106983.
- 8 75. Paluch, P.; Rankin, A. G. M.; Trebosc, J.; Lafon, O.; Amoureux, J. P. Analysis of HMQC  
9 Experiments Applied to a Spin 1/2 Nucleus Subject to Very Large CSA. *Solid State Nucl. Magn. Reson.*  
10 **2019**, *100*, 11-25.
- 11 76. Grey, C. P.; Vega, A. J. Determination of the Quadrupole Coupling-Constant of the Invisible  
12 Aluminum Spins in Zeolite HY with  $^1\text{H}/^{27}\text{Al}$  TRAPDOR NMR. *J. Am. Chem. Soc.* **1995**, *117* (31), 8232-  
13 8242.
- 14 77. Grey, C. P.; Veeman, W. S. The Detection of Weak Heteronuclear Coupling between Spin-1 and  
15 Spin-1/2 Nuclei in MAS NMR;  $^{14}\text{N}/^{13}\text{C}/^1\text{H}$  Triple Resonance Experiments. *Chem. Phys. Lett.* **1992**, *192*  
16 (4), 379-385.
- 17 78. Kalwei, M.; Koller, H. Quantitative Comparison of REAPDOR and TRAPDOR Experiments by  
18 Numerical Simulations and Determination of H-Al Distances in Zeolites. *Solid State Nucl. Magn. Reson.*  
19 **2002**, *21* (3-4), 145-157.
- 20 79. Gan, Z. H. Measuring Nitrogen Quadrupolar Coupling with  $^{13}\text{C}$  Detected Wide-line  $^{14}\text{N}$  NMR  
21 under Magic-Angle Spinning. *Chem. Commun.* **2008**, (7), 868-870.
- 22 80. Duong, N. T.; Nishiyama, Y. Detection of Remote Proton-Nitrogen Correlations by  $^1\text{H}$ -Detected  
23  $^{14}\text{N}$  Overtone Solid-State NMR at Fast MAS. *Phys. Chem. Chem. Phys.* **2022**, *24* (18), 10717-10726.
- 24 81. Jaroszewicz, M. J.; Altenhof, A. R.; Schurko, R. W.; Frydman, L. Sensitivity Enhancement by  
25 Progressive Saturation of the Proton Reservoir: A Solid-State NMR Analogue of Chemical Exchange  
26 Saturation Transfer. *J. Am. Chem. Soc.* **2021**, *143* (47), 19778-19784.
- 27 82. Bak, M.; Rasmussen, J. T.; Nielsen, N. C. SIMPSON: A General Simulation Program for Solid-  
28 State NMR Spectroscopy. *J. Magn. Reson.* **2000**, *147* (2), 296-330.
- 29 83. Tosner, Z.; Vosegaard, T.; Kehlet, C.; Khaneja, N.; Glaser, S. J.; Nielsen, N. C. Optimal Control  
30 in NMR Spectroscopy: Numerical Implementation in SIMPSON. *J. Magn. Reson.* **2009**, *197* (2), 120-  
31 134.
- 32 84. Tosner, Z.; Andersen, R.; Stevenss, B.; Eden, M.; Nielsen, N. C.; Vosegaard, T. Computer-  
33 Intensive Simulation of Solid-State NMR Experiments using SIMPSON. *J. Magn. Reson.* **2014**, *246*, 79-  
34 93.
- 35 85. Brinkmann, A.; Kentgens, A. P. M. Proton-Selective  $^{17}\text{O}$ - $^1\text{H}$  Distance Measurements in Fast  
36 Magic Angle Spinning Solid-State NMR Spectroscopy for the Determination of Hydrogen Bond Lengths.  
37 *J. Am. Chem. Soc.* **2006**, *128* (46), 14758-14759.
- 38 86. Venkatesh, A.; Luan, X.; Perras, F. A.; Hung, I.; Huang, W.; Rossini, A. J.  $t_1$ -Noise Eliminated  
39 Dipolar Heteronuclear Multiple-Quantum Coherence Solid-State NMR Spectroscopy. *Phys. Chem. Chem.*  
40 *Phys.* **2020**, *22*, 20815-20828.
- 41 87. Parella, T. Towards Perfect NMR: Spin-Echo versus Perfect-Echo Building Blocks. *Magn.*  
42 *Reson. Chem.* **2019**, *57* (1), 13-29.
- 43 88. Duong, N. T.; Rossi, F.; Makrinich, M.; Goldbourn, A.; Chierotti, M. R.; Gobetto, R.; Nishiyama,  
44 Y. Accurate  $^1\text{H}$ - $^{14}\text{N}$  Distance Measurements by Phase-Modulated RESPDOR at Ultra-Fast MAS. *J.*  
45 *Magn. Reson.* **2019**, *308*, 106559.
- 46 89. Perras, F. A.; Pruski, M. Reducing  $t_1$  Noise through Rapid Scanning. *J. Magn. Reson.* **2019**, *298*,  
47 31-34.
- 48 90. Atterberry, B. A.; Carnahan, S. L.; Chen, Y.; Venkatesh, A.; Rossini, A. J. Double Echo  
49 Symmetry-Based REDOR and RESPDOR Pulse Sequences for Proton Detected Measurements of  
50 Heteronuclear Dipolar Coupling Constants. *J. Magn. Reson.* **2022**, *336*, 107147.
- 51 91. Ha, K. Crystal structure of bis(pentane-2,4-dionato-kappa O-2,O')platinum(II),  $\text{Pt}(\text{C}_5\text{H}_7\text{O}_2)_2$ . *Z.*  
52 *Kristallogr. NCS* **2011**, *226* (3), 329-330.
- 53  
54  
55  
56  
57  
58  
59  
60

- 1  
2  
3 92. Dechter, J. J.; Kowalewski, J.  $^{195}\text{Pt}$  Spin-Lattice Relaxation and Shielding Anisotropy for  
4  $\text{Pt}(\text{Acac})_2$ . *J. Magn. Reson.* **1984**, *59* (1), 146-149.
- 5 93. Ruddy, D. A.; Jarupatrakorn, J.; Rioux, R. M.; Miller, J. T.; McMurdo, M. J.; Mcbee, J. L.;  
6 Tupper, K. A.; Tilley, T. D. Site-Isolated Pt-SBA15 Materials from Tris(tert-butoxy)siloxy Complexes of  
7 Pt(II) and Pt(IV). *Chem. Mater.* **2008**, *20* (20), 6517-6527.
- 8 94. Goikhman, R.; Aizenberg, M.; Shimon, L. J. W.; Milstein, D. Transition Metal-Catalyzed  
9 Silanone Generation. *J. Am. Chem. Soc.* **1996**, *118* (44), 10894-10895.
- 10 95. Autschbach, J. The Role of the Exchange-Correlation Response Kernel and Scaling Corrections  
11 in Relativistic Density Functional Nuclear Magnetic Shielding Calculations with the Zeroth-Order  
12 Regular Approximation. *Mol Phys* **2013**, *111* (16-17), 2544-2554.
- 13 96. vanLenthe, E.; Snijders, J. G.; Baerends, E. J. The Zero-Order Regular Approximation for  
14 Relativistic Effects: The Effect of Spin-Orbit Coupling in Closed Shell Molecules. *J. Chem. Phys.* **1996**,  
15 *105* (15), 6505-6516.
- 16 97. Davis, J. C.; Buhl, M.; Koch, K. R. On the Origin of  $^{35/37}\text{Cl}$  Isotope Effects on  $^{195}\text{Pt}$  NMR  
17 Chemical Shifts. A Density Functional Study. *J. Chem. Theory Comput.* **2012**, *8* (4), 1344-1350.
- 18 98. Bryce, D. L. NMR Crystallography: Structure and Properties of Materials from Solid-State  
19 Nuclear Magnetic Resonance Observables. *Iucrj* **2017**, *4*, 350-359.
- 20 99. Hodgkinson, P. NMR Crystallography of Molecular Organics. *Prog. Nucl. Magn. Reson.*  
21 *Spectrosc.* **2020**, *118-119*, 10-53.
- 22 100. Gilbert, T. M.; Ziegler, T. Prediction of  $^{195}\text{Pt}$  NMR Chemical Shifts by Density Functional  
23 Theory Computations: The Importance of Magnetic Coupling and Relativistic Effects in Explaining  
24 Trends. *J. Phys. Chem. A* **1999**, *103* (37), 7535-7543.
- 25 101. Frisch, M. J.; Trucks, G. W.; Schlegel, H. B.; Scuseria, G. E.; Robb, M. A.; Cheeseman, J. R.;  
26 Scalmani, G.; Barone, V.; Mennucci, B.; Petersson, G. A.; Nakatsuji, H.; Caricato, M.; Li, X.; Hratchian,  
27 H. P.; Izmaylov, A. F.; Bloino, J.; Zheng, G.; Sonnenberg, J. L.; Hada, M.; Ehara, M.; Toyota, K.;  
28 Fukuda, R.; Hasegawa, J.; Ishida, M.; Nakajima, T.; Honda, Y.; Kitao, O.; Nakai, H.; Vreven, T.;  
29 Montgomery, J. A.; Peralta, J. J. E.; Ogliaro, F.; Bearpark, M.; Heyd, J. J.; Brothers, E.; Kudin, K. N.;  
30 Staroverov, V. N.; Kobayashi, R.; Normand, J.; Raghavachari, K.; Rendell, A.; Burant, J. C.; Iyengar, S.  
31 S.; Tomasi, J.; Cossi, M.; Rega, N.; Millam, J. M.; Klene, M.; Knox, J. E.; Cross, J. B.; Bakken, V.;  
32 Adamo, C.; Jaramillo, J.; Gomperts, R.; Stratmann, R. E.; Yazyev, O.; Austin, A. J.; Cammi, R.; Pomelli,  
33 C.; Ochterski, J. W.; Martin, R. L.; Morokuma, K.; Zakrzewski, V. G.; Voth, G. A.; Salvador, P.;  
34 Dannenberg, J. J.; Dapprich, S.; Daniels, A. D.; Farkas, Ö.; Foresman, J. B.; Ortiz, J. V.; Cioslowski, J.;  
35 Fox, D. J. *Gaussian 09 Version D.01*, Gaussian Inc.: Wallingford, CT, 2009.
- 36 102. te Velde, G.; Bickelhaupt, F. M.; Baerends, E. J.; Guerra, C. F.; Van Gisbergen, S. J. A.; Snijders,  
37 J. G.; Ziegler, T. Chemistry with ADF. *J. Comput. Chem.* **2001**, *22* (9), 931-967.
- 38 103. Sandoval, J. J.; Palma, P.; Alvarez, E.; Campora, J.; Rodriguez-Delgado, A. Mechanism of Alkyl  
39 Migration in Diorganomagnesium 2,6-Bis(imino)pyridine Complexes: Formation of Grignard-Type  
40 Complexes with Square-Planar Mg(II) Centers. *Organometallics* **2016**, *35* (18), 3197-3204.
- 41 104. Su, K.; Tilley, T. D.; Sailor, M. J. Molecular and Polymer Precursor Routes to Manganese-Doped  
42 Zinc Orthosilicate Phosphors. *J. Am. Chem. Soc.* **1996**, *118* (14), 3459-3468.
- 43 105. Smith, D. C.; Haar, C. M.; Stevens, E. D.; Nolan, S. P.; Marshall, W. J.; Moloy, K. G. Synthetic,  
44 Structural, and Solution Calorimetric Studies of  $\text{Pt}(\text{CH}_3)_2(\text{PP})$  Complexes. *Organometallics* **2000**, *19* (7),  
45 1427-1433.
- 46 106. Searles, K.; Siddiqi, G.; Safonova, O. V.; Coperet, C. Silica-Supported Isolated Gallium Sites as  
47 Highly Active, Selective and Stable Propane Dehydrogenation Catalysts. *Chem. Sci.* **2017**, *8* (4), 2661-  
48 2666.
- 49 107. Yanai, T.; Tew, D. P.; Handy, N. C. A New Hybrid Exchange-Correlation Functional using the  
50 Coulomb-Attenuating Method (CAM-B3LYP). *Chem. Phys. Lett.* **2004**, *393* (1-3), 51-57.
- 51 108. Rassolov, V. A.; Pople, J. A.; Ratner, M. A.; Windus, T. L. 6-31G\* Basis Set for Atoms K  
52 through Zn. *J. Chem. Phys.* **1998**, *109* (4), 1223-1229.
- 53  
54  
55  
56  
57  
58  
59  
60

- 1  
2  
3 109. Roy, L. E.; Hay, P. J.; Martin, R. L. Revised Basis Sets for the LANL Effective Core Potentials. *J. Chem. Theory Comput.* **2008**, *4* (7), 1029-1031.
- 4  
5 110. vanLenthe, E.; vanLeeuwen, R.; Baerends, E. J.; Snijders, J. G. Relativistic Regular Two-  
6 Component Hamiltonians. *Int. J. Quantum Chem.* **1996**, *57* (3), 281-293.
- 7 111. Zurek, E.; Pickard, C. J.; Autschbach, J. Density Functional Study of the  $^{13}\text{C}$  NMR Chemical  
8 Shifts in Single-Walled Carbon Nanotubes with Stone-Wales Defects. *J. Phys. Chem. C* **2008**, *112* (31),  
9 11744-11750.
- 10 112. Clark, S. J.; Segall, M. D.; Pickard, C. J.; Hasnip, P. J.; Probert, M. J.; Refson, K.; Payne, M. C.  
11 First Principles Methods using CASTEP. *Z. Kristallogr.* **2005**, *220* (5-6), 567-570.
- 12 113. Perdew, J. P.; Burke, K.; Ernzerhof, M. Generalized Gradient Approximation Made Simple.  
13 *Phys. Rev. Lett.* **1996**, *77* (18), 3865-3868.
- 14 114. Tkatchenko, A.; Scheffler, M. Accurate Molecular Van Der Waals Interactions from Ground-  
15 State Electron Density and Free-Atom Reference Data. *Phys. Rev. Lett.* **2009**, *102* (7), 073005.
- 16 115. van Meerten, S. G. J.; Franssen, W. M. J.; Kentgens, A. P. M. ssNake: A Cross-Platform Open-  
17 Source NMR Data Processing and Fitting Application. *J. Magn. Reson.* **2019**, *301*, 56-66.
- 18 116. Oas, T. G.; Griffin, R. G.; Levitt, M. H. Rotary Resonance Recoupling of Dipolar Interactions in  
19 Solid-State Nuclear Magnetic-Resonance Spectroscopy. *J. Chem. Phys.* **1988**, *89* (2), 692-695.
- 20 117. Venkatesh, A.; Hung, I.; Boteju, K. C.; Sadow, A. D.; Gor'kov, P. L.; Gan, Z.; Rossini, A. J.  
21 Suppressing  $^1\text{H}$  Spin Diffusion in Fast MAS Proton Detected Heteronuclear Correlation Solid-State NMR  
22 Experiments. *Solid State Nucl. Magn. Reson.* **2020**, *105*, 101636.
- 23 118. Herzfeld, J.; Berger, A. E. Sideband Intensities in NMR Spectra of Samples Spinning at the  
24 Magic Angle. *J. Chem. Phys.* **1980**, *73* (12), 6021-6030.
- 25 119. Eichele, K. *HBA 1.7.5*, Universität Tübingen, 2015.
- 26 120. Fung, B. M.; Khitritin, A. K.; Ermolaev, K. An Improved Broadband Decoupling Sequence for  
27 Liquid Crystals and Solids. *J. Magn. Reson.* **2000**, *142*, 97-101.
- 28  
29  
30  
31  
32  
33  
34  
35  
36  
37  
38  
39  
40  
41  
42  
43  
44  
45  
46  
47  
48  
49  
50  
51  
52  
53  
54  
55  
56  
57  
58  
59  
60